JOURNAL OF GEOPHYSICAL RESEARCH: OCEANS, VOL. 118, 1587–1605, doi:10.1002/jgrc.20146, 2013

Wave-current interactions in a wave-dominated tidal inlet

Guillaume Dodet,[1,2] Xavier Bertin,[2] Nicolas Bruneau,[1,3] André B. Fortunato,[1] Alphonse Nahon,[1] and Aron Roland[4]

Received 12 October 2012; revised 19 February 2013; accepted 25 February 2013; published 28 March 2013.

[1] Wave-current interactions play a major role in the dynamics of shallow tidal inlets. This study investigates these interactions at a natural inlet, with a strong focus on current-induced changes on wave propagation. The analysis of hydrodynamic data collected at the Albufeira lagoon, Portugal, revealed spatiotemporal variations of water levels and wave heights along the inlet, attributed to wave-current interaction processes. We compared the simulations of a coupled wave-circulation modeling system, computed with and without waves, and propagated with and without current feedback. The wave-induced setup inside the lagoon represented 7%–15% of the offshore significant wave height. The accuracy of the wave's predictions improved when current feedback was included. During ebb, the currents increased the wave height at the mouth of the inlet (up to 20%) and decreased the wave height in the inlet (up to 40%), due to current-induced refraction, steepness dissipation, and partial blocking. During flood, the currents decreased the wave height in the inlet (up to 10%) and increased the wave height at the exterior parts of the ebb shoal (up to 10%), due to current-induced refraction. These effects significantly attenuate seaward sediment fluxes during ebb and contribute to the sediment accretion in the inlet.

Citation: Dodet, G., X. Bertin, N. Bruneau, A. B. Fortunato, A. Nahon, and A. Roland (2013), Wave-current interactions in a wave-dominated tidal inlet, *J. Geophys. Res. Oceans*, *118*, 1587–1605, doi: 10.1002/jgrc.20146.

1. Introduction

[2] Coastal lagoons are of great ecological and socio-economic importance given their privileged location at the land-ocean interface. Tidal inlets, which connect the open ocean with a back-barrier lagoon, constitute navigation routes and enable fish and larvae migrations, nutrient exchanges, and maintenance of water quality and salinity levels in the lagoon water. Wave-dominated tidal inlets are constantly adapting to the oceanic forcing, and large morphological responses may occur very rapidly. In order to predict accurately such morphological changes, it is essential to understand well the processes that govern the circulation in the inlet. Thus, improving our knowledge on wave-current interactions in tidal inlets is one of the key requirements toward an effective and sustainable management framework for coastal lagoons.

[3] Early work on tidal inlets investigated the relationship between several characteristics of tidal inlets such as tidal prism, inlet cross sectional area, or lagoon surface area [*O'Brien*, 1992, 1969; *Vincent and Corson*, 1980] and led to empirical and conceptual theories still widely used. Other authors [*Brown*, 1928; *Keulegan*, 1967; *Mota Oliveira*, 1970] used simplified approaches of steady-flow hydraulics to formulate analytical solutions to investigate the currents in the channel and the tide modulation in the associated lagoon. *Hayes* [1975, 1979] proposed a classification of tidal inlets based on local yearly averaged tidal range and wave regime. More recently, numerical models have been applied to a broad range of natural tidal inlets, from large mixed-energy tide-dominated inlets [*Cayocca*, 2001, *Elias et al*., 2006] to smaller wave-dominated inlets [*Ranasinghe et al*., 1999; *Bertin et al*., 2009; *Malhadas et al*., 2009; *Tung et al*., 2009; *Bruneau et al*., 2011] and synthetic tidal inlets [*Hench and Luettich*, 2003; *Malhadas et al*., 2009; *Nahon et al*., 2012a], in order to obtain detailed information on the main processes driving circulation and sediment dynamics.

[4] The hydrodynamics of wave-dominated tidal inlets, when freshwater inflow is negligible, is controlled mainly by the combined effect of tides and waves. The ebb and flood currents interact with the incident wavefield to give rise to complex patterns of currents and waves in the vicinity of the inlet mouth and adjacent beaches. The mechanism of such interactions in a two-dimensional framework was formulated by *Longuet-Higgins and Stewart* [1964] who introduced the radiation stress concept and proved the existence of the momentum transfer between waves and currents. Later, *Bretherton and Garrett* [1969] formulated the wave action equation for directional wave spectra in slowly varying media, and *Huang et al*. [1972] described the effects of

[1]Estuaries and Coastal Zones Division, National Laboratory of Civil Engineering, Lisbon, Portugal.
[2]UMR 7266 LIENSs CNRS-Université de La Rochelle, Coastal and Environment Institute, La Rochelle, France.
[3]British Antarctic Survey, Cambridge, UK.
[4]Institute for Hydraulic and Water Resources Engineering, Technische Universität Darmstadt, Darmstadt, Germany.

Corresponding author: G. Dodet, UMR LIENSS 7266, Coastal and Environment Institute, 2 Rue Olympe de Gouges, 17000 La Rochelle Cedex, France. (gdodet01@univ-lr.fr)

2169-9275/13/10.1002/jgrc.20146

currents on the wave energy spectral shape. Several experimental studies were conducted in wave flumes [e.g., *Thomas*, 1981; *Lai et al*., 1989; *Chawla and Kirby*, 2002] or offshore basins [e.g., *Guedes Soares and de Pablo*, 2006] to investigate the evolution of wave characteristics under the influence of currents. In particular, the process of wave blocking when a wavefront encounters a strong facing current has been the subject of several studies [*Lai et al*., 1989; *Chawla and Kirby*, 2002; *Suastika*, 2012) but remains only partially understood. Observations of the effects of currents on waves in natural environments are also mentioned in several studies [*Wolf and Prandle*, 1999; *Rusu et al*., 2011, *Westhuysen*, 2012], yet they are still too sparse to give a significant overview of this mechanism in complex coastal systems such as tidal inlets. Based on the results of a fully coupled ocean-atmosphere-wave-sediment transport modeling system, *Olabarrieta et al.* [2011] identified the effects of wave-current interactions on the circulation of Willapa Bay (Washington State). The attempts of morphodynamic modeling of tidal inlets in energetic environments, although they provided encouraging results [*Ranasinghe et al*., 1999; *Cayocca*, 2001; *Bertin et al*., 2009; *Bruneau et al*., 2011], still suffer from inaccuracies. To this day, only a few authors managed to reproduce the closure of shallow inlets [*Ranasinghe and Pattiaratchi*, 1999, *Tung et al.* 2009], yet the forcing mechanisms remain only partially understood and still require further research.

[5] This paper investigates the hydrodynamics of a wave-dominated tidal inlet system located on the western coast of Portugal through in situ data analysis and numerical simulations provided by a wave-current modeling system. The tidal inlet of the Albufeira Lagoon is a very dynamic environment subjected to a meso-tidal regime and an energetic wave climate, which together lead to fast morphological changes, such as channel migration and inlet closure. The following section describes the field work that took place in September 2010 during which hydrodynamic and topographic data were collected. The third section describes the modeling system implemented to investigate the circulation in wave-dominated environments. The hydrodynamics of the inlet is described in section 4 through the analysis of field data and model results and cross-comparisons between them. In section 5, the effects of wave-current interactions on the inlet hydrodynamics are discussed and their effects on the sediment transport are analyzed. Some limitations of the present study are also presented in this section. The paper concludes with a summary of the main findings and gives some perspectives for future work.

2. Field Experiment

2.1. Study Site

2.1.1. Geomorphological Setting

[6] The Albufeira Lagoon is located on the west coast of Portugal, on the western edge of the Setúbal Peninsula, around 20 km south of Lisbon (Figure 1). The width of the continental shelf along the Caparica-Espichel littoral arc ranges from 40 km, at the mouth of the Tagus estuary, to 5 km, in front of the lagoon where the Lisbon Canyon crosscuts the shelf. The lagoon covers an elongated surface area of 1.3 km^2 whose principal axis follows a SW-NE orientation, slightly oblique to the coast. The system comprises two main bodies: the small and shallow (~5 m deep) *Lagoa Pequena* at the inland extremity and the wider and deeper (~15 m deep) *Lagoa Grande* [*Freitas and Ferreira*, 2004]. The latter is connected to the sea by a narrow inlet (a few dozens of meters wide), which may undergo fast morphological changes on weekly to monthly time scales [*Nahon et al*., 2012b]. More particularly, the inlet morphology presents a seasonal behavior leading to its quasi-systematic natural closure during winter, after which it is artificially open in spring. These anthropogenic interventions, dating back to at least the mid-15th century [*Freitas and Ferreira*, 2004], have preserved the ecological and economic role of this coastal system to this day. This part of the coast is characterized by steep beaches with medium to coarse sediment. During the field campaign, the average beach slope was 0.12 and the median grain size ranged between 0.0007 and 0.0018 m [*Bosnic et al*., 2011].

2.1.2. Hydrodynamic Setting

[7] The western Portuguese coast, with semidiurnal tides ranging from less than 1 to more than 3.5 m, can be considered as a meso-tidal environment, according to Davies' classification [*Davies*, 1964]. When tides propagate into the lagoon, the semidiurnal tidal constituents are damped, whereas quarter-diurnal and fortnightly nonlinear constituents develop [*Mehta and Özsöy*, 1978], resulting in a strongly distorted signal. The tidal amplitude in the lagoon can exhibit

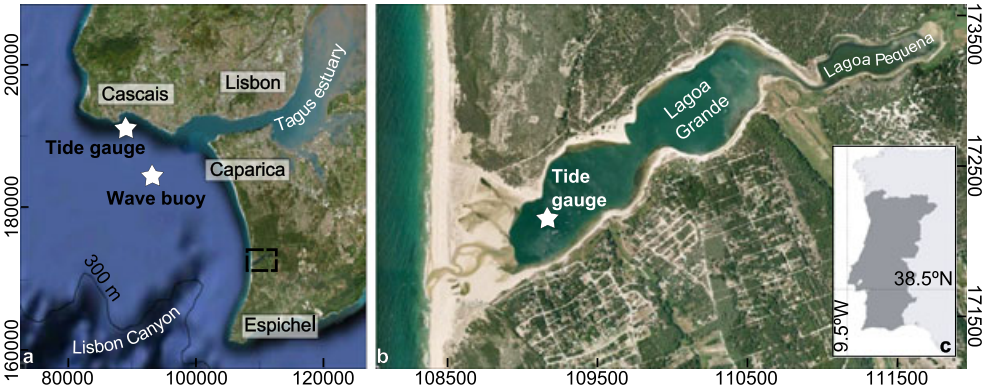

Figure 1. The Albufeira Lagoon: (a) location along the Caparica-Espichel littoral arc (black rectangle), (b) aerial photograph and (c) location on a map of Portugal. On Figures 1a and 1b: place names, geomorphological features, and data stations (stars).

significant seasonal variations. Indeed, this amplitude is negatively correlated with the head losses along the inlet channel, which are generally low at the end of summer, during which waves are small and sediments are flushed out from the channel. During winter, the wave climate becomes more energetic and promotes the landward sediment transport through the channel which reduces the inlet cross-section. This reduction decreases the tidal prism sometimes until the inlet closure. The migration of the inlet mouth, and the corresponding lengthening of the inlet channel, can also increase the head losses and reduce the tidal amplitudes. A similar behavior was observed further north on the Portuguese coast at the Óbidos lagoon by *Oliveira et al*. [2006]. This seasonal behavior is illustrated in Figure 2 with the evolution of the amplitude of the semidiurnal constituents M2 and M4 deduced from a 1 month sliding window harmonic analysis of a 7 month time series of sea surface elevation measured by a tide gauge located in the *Lagoa Grande* (Figure 1b). Both the temporal and spatial variations of the tide in the Albufeira Lagoon were investigated by *Freitas and Andrade* [1994], who obtained ratios of lagoon/oceanic tidal amplitude ranging from 8% to 43% and differences between ebb and flood duration varying from 2 to 4 h (the ebb duration being always longer), depending on the morphological stage of the inlet. *Freitas and Ferreira* [2004] reported a maximum tidal prism of 1.57×10^6 m^3 and *Nahon et al*., [2012b] used modeled mean wave parameters and elevation in front of the Albufeira Lagoon to compute a gross littoral drift of 316400 m^3 for an 8 month period. These values indicate that the Bruun stability criterion [*Bruun*, 1966] is very low (<10), and confirm the fact that the morphology of the Albufeira lagoon inlet is wave dominated.

[8] The wave regime off the Portuguese west coast is dominated by long-period swells generated in the North Atlantic Ocean. During the winter period, severe wind seas may occasionally prevail, when the path of a low-pressure system reaches the Iberian Peninsula. A study based on the analysis of a 57 year time series of hindcasted mean-wave parameters [*Dodet et al*., 2010], computed with the WAVEWATCH III (WW3) wave model [*Tolman*, 2009], revealed that the mean annual deep water significant wave height (HS), mean direction (MWD), and peak period (TP) 100 km off the Albufeira Lagoon (10.0°W, 38.0°N, ~ 3000 m deep) were respectively 1.9 m, 10.5 s, and 312°. During winter (respectively summer), the corresponding values were 2.5 m, 12.1 s, and 305° (respectively 1.3 m, 8.4 s, and 319°). These values are consistent with other studies of the wave climate in Portugal based on observations [*Pires and Pessanha*, 1986; *Costa et al*., 2001].

[9] The drainage basin of the Albufeira Lagoon covers a surface area of around 106 km^2, with four main rivers flowing into the eastern part of the lagoon. However, even the larger rivers only have a significant water flow during years of exceptional precipitation [*Freitas and Ferreira*, 2004], and the contribution of freshwater discharge to the inlet hydrodynamics is negligible. *Freitas* [1995] reported that the discharge of the two main rivers that flow into the lagoon is zero during the summer months and maximal between December and April after periods of intense precipitations. However, monthly means of river discharge between 1986 and 1989 never exceeded 0.25 m^3 s^{-1}. For the months of September and October, this value was always lower than 0.1 m^3 s^{-1}. The consequences of freshwater inflow will thus not be discussed in the present paper nor considered in the simulations.

2.2. Field Work Description

2.2.1. Atmospheric and Hydrodynamic Conditions

[10] The field experiment took place on 23–24 September 2010, during spring tides. This period of the year corresponds generally with a good hydraulic efficiency of the inlet and the first energetic oceanic swells of the pre-winter season. During this campaign, anticyclonic conditions prevailed, with high atmospheric pressures (1018−1022 hPa) and light-to-moderate breeze (mean wind velocity ~3 m s^{-1}). The tidal ranges measured at Cascais (tide gauge location in Figure 1a) for the three tidal cycles were respectively 2.55, 2.51, and 2.61 m. The wave events resulted from the succession of a dying 12 s NW swell and a 20 s WNW swell generated a week earlier near the Bermuda Islands when Hurricane Igor began to develop into an extratropical cyclone. During the 2 days of the campaign, HS in front of the inlet (~150 m water depth) increased from 1.1 to 1.8 m, TP shifted from 10 to 22 s while MWD rotated from WNW to W (Figure 3).

2.2.2. Instruments Deployment

[11] Figure 4 shows the locations of the instruments as well as the topography of the tidal inlet and the adjacent barrier beaches. Two pressure transducers (PT; Level TROLL

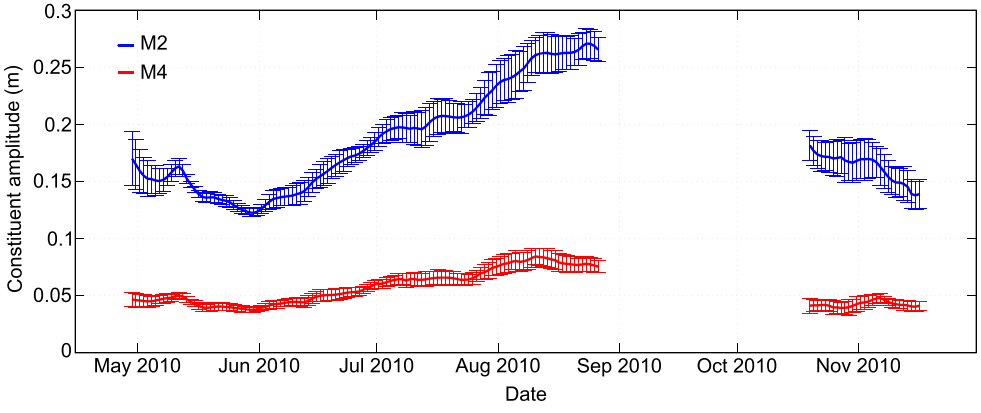

Figure 2. Amplitudes and 95% confidence intervals for the tidal constituents M2 (blue) and M4 (red) in the lagoon between April and December 2010.

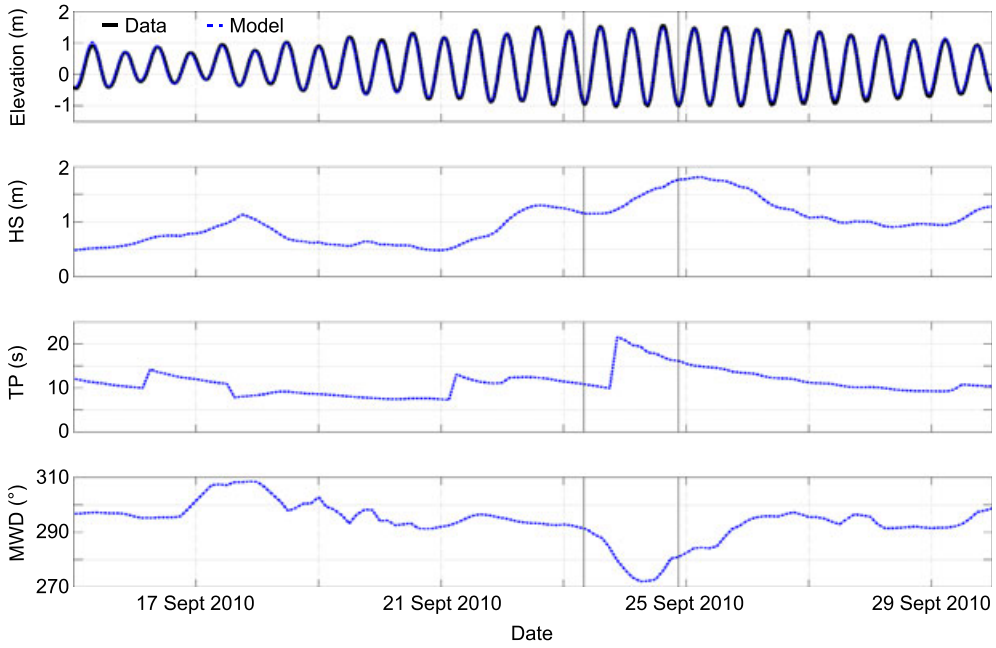

Figure 3. Hydrodynamics conditions between 15 and 30 September 2010. (first panel) Sea surface elevation at Cascais (data and model); (second panel) significant wave height; (third panel) peak period; and (fourth panel) mean wave direction. The mean wave parameters were computed in front of the inlet 5 km off the coast at 150 m water depth.

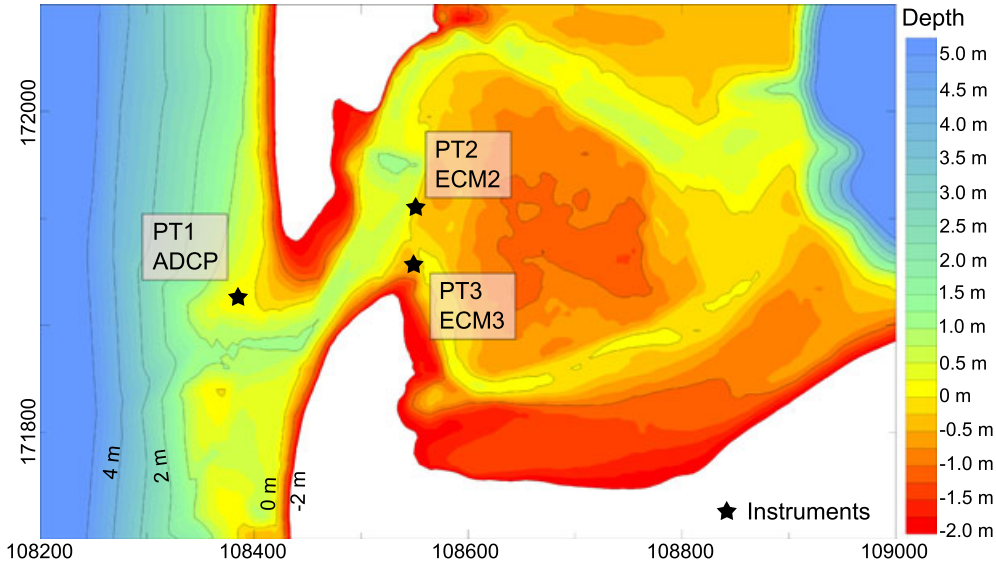

Figure 4. Topography of the inlet on 23 September 2010, positions of the instruments (ADCP: Acoustic Doppler Current Profiler; PT: Pressure Transducer; ECM: Electromagnetic Current-Meter).

500, In-Situ Inc.), two electromagnetic current-meters (ECM; INFINITY-EM, JFE Advantech Co., Ltd.), and one acoustic Doppler current profiler with an integrated pressure sensor (ADCP; Aquadopp Profiler 2MHz, Nortek AS) were synchronized and deployed during the morning low tide of 23 September. Two scaffold frames, each comprises one PT and one ECM, were installed along the main channel: one on the seaward flank of the flood delta and the other one on a small sand spit along the main channel bypassed by a secondary channel. Both arrays recorded pressure variations and local currents at a 2 Hz frequency of acquisition. The ADCP was fixed on top of a robust steel stake ending with a large screw, which was buried on the flat part of an ebb shoal connected to the northern barrier beach. Pressure and current profiles were sampled continuously at 1 Hz. Meanwhile, the inlet area was surveyed using

two Real Time Kinematic GPS and one Differential GPS. The deployment ended on the evening low tide of 24 September, after the completion of three tidal cycles. The measured topography, which includes the inlet principal and secondary channels, the flood-tidal delta, the barrier, and the intertidal area of adjacent beaches and ebb-tidal delta, was complemented with bathymetric measurements realized in March 2010 with an onboard echo sounder.

2.2.3. Data Processing

[12] In order to analyze the data and compare them with the model outputs, the instruments records were processed as follows: (1) the pressure records were converted into time series of sea surface elevation, assuming hydrostaticity; (2) the raw time series of elevation and velocities were smoothed by a 10 min running average, in order to filter out the contribution of the short waves; (3) for each PT, a Fourier transform was applied to consecutive 10 min windows of elevation data, and a correction factor was applied to each spectral bin of the computed energy density spectrum ($S(f)$) to take into account the pressure attenuation. Then HS was calculated by integrating $S(f)$ over the frequency range $0.035 < f < 0.5$ Hz, where f is the frequency, and TP was computed as the frequency bin containing the maximum energy density. The lower bound (0.035 Hz) was chosen intentionally low to capture most of the energy of the very long swell that reached the Portuguese shores on 24 September. The choice of the higher bound was constrained by the instruments minimum acquisition rate (1 Hz) and its corresponding Nyquist frequency (0.5 Hz). The formula to compute HS is

$$HS = 4\sqrt{\int S(f)\mathrm{d}f} \tag{1}$$

3. The Modeling System

3.1. Description of the Modeling System

[13] The modeling system that is being developed aims to simulate the hydrodynamics and non-cohesive sediment dynamics in estuaries and coastal inlets under the effect of tides and waves. The core model of the system is the hydrodynamic model SELFE [*Zhang and Baptista*, 2008]. The Simulating WAves Nearshore (SWAN) spectral wave model [*Booij et al*., 1999] was coupled to SELFE and several wave-induced processes were implemented to reproduce the circulation induced by the waves. For the purpose of this study, the morphodynamic module was not used and thus will not be described hereafter.

3.1.1. The SWAN Wave Module

[14] The spectral wave model SWAN solves the wave action equation that describes the evolution of the wave spectrum in time, geographical, and spectral spaces. In most spectral models, wave action density N is preferred over wave energy E ($E = \sigma.N$, where σ is the intrinsic angular frequency) since it is a conserved quantity in the presence of currents, unlike the energy density [*Bretherton and Garrett*, 1969]. In the presence of currents, the wave action density balance equation can be written as

$$\frac{\partial N}{\partial t} + \nabla[\vec{c}N] + \frac{\partial}{\partial\sigma}c_\sigma N + \frac{\partial}{\partial_\theta}c_\theta N = \frac{S}{\sigma} \tag{2}$$

$$\vec{c} = \frac{dw}{dk} = \overrightarrow{c_g} + \vec{U} = \frac{1}{2}\left[\left(1 + \frac{2kd}{\sinh 2kd}\right)\right]\frac{\sigma\vec{k}}{k^2} + \vec{U} \tag{3}$$

$$c_\sigma = \frac{\partial\sigma}{\partial d}\left(\frac{\partial H}{\partial t} + \vec{U}\cdot\nabla H\right) - c_g\vec{k}\cdot\frac{\partial\vec{U}}{\partial s} \tag{4}$$

$$c_\theta = -\frac{1}{k}\left(\frac{\partial\sigma}{\partial H}\frac{\partial H}{\partial m} + \vec{k}.\frac{\partial\vec{U}}{\partial m}\right) \tag{5}$$

where $\vec{c}$ is the advection velocity vector in the geographical space (defined in equation (3)), c_σ and c_θ are the advection velocities in the spectral space (defined in equations (4) and (5), respectively), σ is the relative (intrinsic) radian frequency, θ is the spectral direction, S represents the source terms, ω is the absolute radian frequency, $\vec{k}$ is the wave number vector, $\overrightarrow{c_g}$ is the wave group velocity vector, $\vec{U}(Ux, Uy)$ is the ambient current, H is the mean water depth, s is a coordinate in the direction θ, and m is a coordinate perpendicular to s. The terms on the left-hand side of (2) represent respectively the change of wave action in time, the propagation of wave energy in two-dimensional geographical space, the shifting of the intrinsic frequency due to variations in depth and mean currents, and the depth- and current-induced refraction. The right-hand side is the source/sink term that represents all physical processes which generate, dissipate, or redistribute wave energy. These processes include wind input, whitecapping dissipation, nonlinear quadruplet and triad interactions, bottom friction, depth-induced wave breaking, and diffraction.

3.1.2. The SELFE Hydrodynamic Module

[15] The SELFE model (semi-implicit Eulerian-Lagrangian finite-element model) is designed to compute unsteady baroclinic circulations across river-to-ocean scales. SELFE solves the two-dimensional (depth-averaged, 2-DH) or three-dimensional (3-D) shallow-water equations, with Boussinesq approximations, and transport equations for salt and heat. The model runs on unstructured horizontal grids with hybrid vertical coordinates (partly terrain-following S coordinates and partly Z coordinates). Extensive information about the model can be found in *Zhang and Baptista* [2008]. The source code of SELFE was modified in order to take into account the effect of short waves on the hydrodynamics. In this study, the recently developed depth-averaged version of the code was used [*Zhang et al*., 2009]. The two components of the forcing induced by the gradients of wave radiation stresses are computed by SWAN as

$$F_x = -\frac{\partial S_{xx}}{\partial x} - \frac{\partial S_{xy}}{\partial y} \tag{6}$$

$$Fy = -\frac{\partial S_{xy}}{\partial x} - \frac{\partial S_{yy}}{\partial y} \tag{7}$$

where S_{xx}, S_{xy} and S_{xy} are the radiation stresses [*Longuet-Higgins and Stewart*, 1964; *Battjes*, 1972]:

$$S_{xx} = \rho g \int \left[n\cos^2\theta + n - \frac{1}{2} \right] E \, \mathrm{d}\sigma \mathrm{d}\theta \tag{8}$$

$$S_{xy} = S_{yx} = \rho g \int n\sin\theta\cos\theta E \, \mathrm{d}\sigma \mathrm{d}\theta \tag{9}$$

$$S_{yy} = \rho g \int \left[n\sin^2\theta + n - \frac{1}{2} \right] E \, \mathrm{d}\sigma \mathrm{d}\theta \tag{10}$$

where n is the group velocity over the phase velocity, g is the Earth gravity acceleration, and ρ is the water density. Finally, the hydrodynamic system of equations can be written as follows:

$$\frac{\partial \eta}{\partial t} + \frac{\partial HU_x}{\partial x} + \frac{\partial HU_y}{\partial y} = 0 \tag{11}$$

$$\frac{DU_x}{Dt} = -g\frac{\partial \eta}{\partial x} + \frac{F_x}{\rho H} - \frac{Cd}{H}\sqrt{U_x^2 + U_y^2}U_x + fU_y + \frac{\partial}{\partial x}\left(\nu \frac{\partial Ux}{\partial x}\right) + \frac{\partial}{\partial y}\left(\nu \frac{\partial U_x}{\partial y}\right) \tag{12}$$

$$\frac{DU_y}{Dt} = -g\frac{\partial \eta}{\partial y} + \frac{F_y}{\rho H} + \frac{Cd}{H}\sqrt{U_x^2 + U_y^2}U_y - fU_x + \frac{\partial}{\partial x}\left(\nu \frac{\partial U_y}{\partial x}\right) + \frac{\partial}{\partial y}\left(\nu \frac{\partial U_y}{\partial y}\right) \tag{13}$$

where $\frac{D}{Dt}$ is the total derivative, η is the free surface elevation, ν is the horizontal turbulent eddy viscosity coefficient computed according to *Battjes* [1975], and C_d is the bottom drag coefficient. The computation of C_d is based on the combined waves and current bed shear stress formula given by *Soulsby* [1997]:

$$\tau_m = \tau_c \left[1 + 1.2\left(\frac{\tau_w}{\tau_c + \tau_w} \right)^{3.2} \right] \tag{14}$$

in which τ_m, τ_w, and τ_c are respectively the total bed shear stress, the wave-induced shear stress, and the current-induced shear stress. The rough bed friction factor used to compute τ_w is calculated according to *Swart* [1974]. Friction due to bed forms was also taken into account through a form-drag component in the computation of the roughness length z_0, taken as the maximum of the wave-induced [*Nielsen*, 1992] and current-induced form-drag component [*Van Rijn*, 1984].

3.1.3. Module Coupling

[16] The wave module and the hydrodynamic module run sequentially and communicate with each other through a Python routine. The mean wave parameters and the forcing terms associated to the wave radiation stresses computed by SWAN in stationary mode are read and interpolated by SELFE on its unstructured grid. Then the wave-induced turbulent eddy viscosity is computed. When the hydrodynamic simulation is accomplished, both elevation and current fields are averaged over the duration of the simulation to limit variations in the current field read by SWAN from one simulation to another and interpolated on the rectilinear SWAN grid. Finally, the wave model is run with the feedback of these new elevation and current inputs.

3.2. Modeling Setup

[17] The implementation of the modeling system in the Albufeira Lagoon involved three nested grids (two coarse regular grids and one fine rectilinear grid) for the wave model and one unstructured grid for the circulation model. Although the recent versions of SWAN (V40.85, V40.91) allow the use of a single unstructured grid, the nesting strategy was faster. The spatial resolutions of the different domains are given in Table 1 and their extents are shown in Figure 5. This domains' setting was defined so that optimal computation time meets the high resolution (~1 m) required to accurately reproduce the flow and the wave propagation in the narrow channels and the wave-breaking dissipation over the steep slope of the beach. The waves were updated every 5 min in order to avoid abrupt variations in the water level and currents read by SWAN, from one simulation to another.

[18] The first grid of the wave model was forced at its external boundaries by 10 km spaced wave spectra generated by the WW3 regional model implemented for the North-East Atlantic Ocean by *Dodet et al*. [2010]. Each nested grid read the forcing wave spectra computed by its "mother" grid and ran sequentially to provide spectral forcing for its "child" grid. The six-hourly ERA-Interim wind fields [*Dee et al*., 2011] were used to force the wave models. The spectral grids for the regional (WW3) and local wave models (SWAN) used 30 regularly spaced directions and 40 frequencies exponentially spanning the 0.03–0.5 Hz range. The water level provided in the SWAN model was uniform for the two coarse grids and corresponded to the water level computed by SELFE at the previous iteration at an offshore location (~20 m deep), while the finest grid used the space-variable elevation field computed by SELFE. The physical processes taken into account in the wave model were whitecapping dissipation [*Westhuysen et al*., 2007], including an enhanced dissipation term for breaking dissipation on negative current gradients [*Westhuysen*, 2012] whose calibration coefficient was set at 5, bottom friction (default Madsen coefficient, 0.05), depth-induced breaking (constant breaker height to water depth ratio $\gamma = 0.73$), and quadruplet and triad wave-wave interactions. Spectral outputs, computed in the fixed frame, were retrieved after each run (every 5 min) and were used to compute both HS and TP (according to equation (1)). The time series of HS and TP were then interpolated on the same time index as the data.

[19] The SELFE ran in 2-D barotropic mode on an unstructured triangular grid. The resolution of the grid is maximal (3.5 m) in the channel and along the beaches adjacent to the inlet, where the currents are strong and the depth and current gradients are the largest. The grid extension (dashed black line in Figure 4) covers in particular the

Table 1. Computational Grids of the Modeling System

Grid	Type	Nodes	Resolution (m)	
			Min.	Max.
SWAN1	Regular	1360	1000	1000
SWAN2	Regular	756	200	200
SWAN3	Rectilinear	5720	90	2.5
SELFE	Triangular	28832	1000 [a]	3.5 [a]

[a]The resolution corresponds to the mean length of the sides of the triangle.

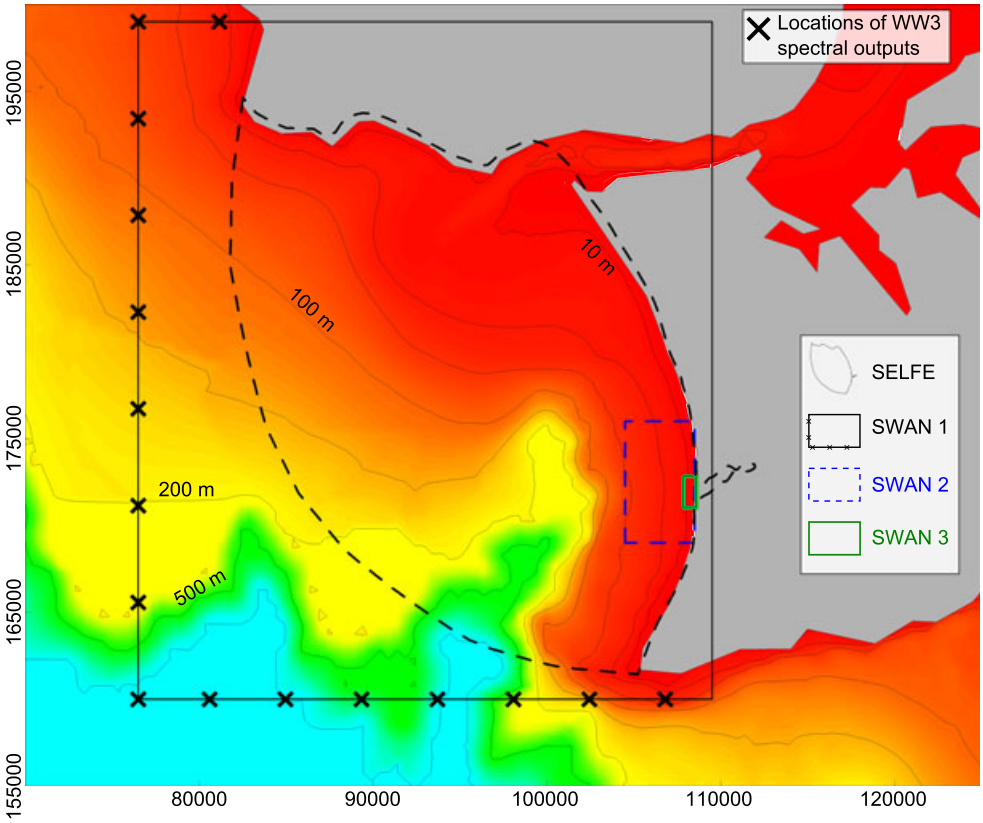

Figure 5. Limits of the computational grids of the hydrodynamic model (SELFE) and the wave models (SWAN 1, SWAN 2, and SWAN 3), locations of the WW3 spectra and bathymetry.

whole surface area of the inlet-lagoon system, including a dry zone like barrier dunes and surrounding lands. The wetting/drying algorithm for shallow areas in SELFE allows the intertidal zone to be alternatively wet or dry whether the total depth at the nodes is above or below a specified minimum depth (1 cm here). The model was forced at its ocean boundary by 16 tidal constituents whose amplitude and phase were computed with the regional model of *Bertin et al.* [2012]. The upstream boundary in the lagoon was defined as a closed boundary since freshwater inflow is negligible (cf. section 2.1.2.). Five day simulations, including a 1 day ramp-up, with a hydrodynamic time step of 20 s produced outputs of sea surface elevation, velocities, and variance density spectra, saved every 5 min over the domain. The coefficient of *Battjes* [1975] for wave-induced eddy viscosity was set to 0.5. Three configurations of the modeling system were defined for this study: *config.1* refers to a simulation with no wave; *config.2* refers to a simulation with waves, when the wave model reads the elevation field computed by the circulation model but does not read the current field; and *config.3* refers to a simulation with waves, when the wave model reads both the elevation and the current field computed by the circulation model. The effect of the wave radiation stresses on the circulation was included in both *config.2* and *config.3*.

4. Inlet Hydrodynamics

[20] This section describes the external forcing that controls the dynamics of the Albufeira Lagoon as well as the hydrodynamic conditions at the inlet during the field campaign. Both numerical results and data time series were analyzed and compared in order to highlight the main characteristics of the inlet hydrodynamics.

4.1. Incident Forcing

[21] The model results were compared to a data set of sea surface elevation and wave parameters representative of the off-shore conditions in order to validate the forcing used to feed the model. The data used to validate the incident modeled tide are a 1 year (2010) time series of tide gauge measurements at the Cascais marina (Figure 1a). After harmonic analysis was applied to the data, a 1 month synthetic tide was reconstructed from the 16 main computed amplitudes and phases and compared to the modeled elevation at the corresponding period and location (Figure 3, first panel). The comparison between model and data showed an excellent agreement, with a root mean squared error (RMSE) of 0.02 m. The modeled elevation was also compared directly to the measured elevation in order to estimate the contribution of the atmospheric forcing. For the entire month, the RMSE was 0.06 m, and for the 2 days of the campaign, the RMSE was 0.04 m.

[22] The modeled HS, MWD, and TP were compared to a 4 month time series of wave data measured by a Triaxys buoy located at the entrance of the Tagus estuary (Figure 6, see Figure 1a for the buoy location). The respective RMSE was 0.29 m, 20.0°, and 1.83 s, and the scatter index (SI) was 17.6% and 15.9%, for HS and TP respectively. Since no data were available at this wave buoy during the field

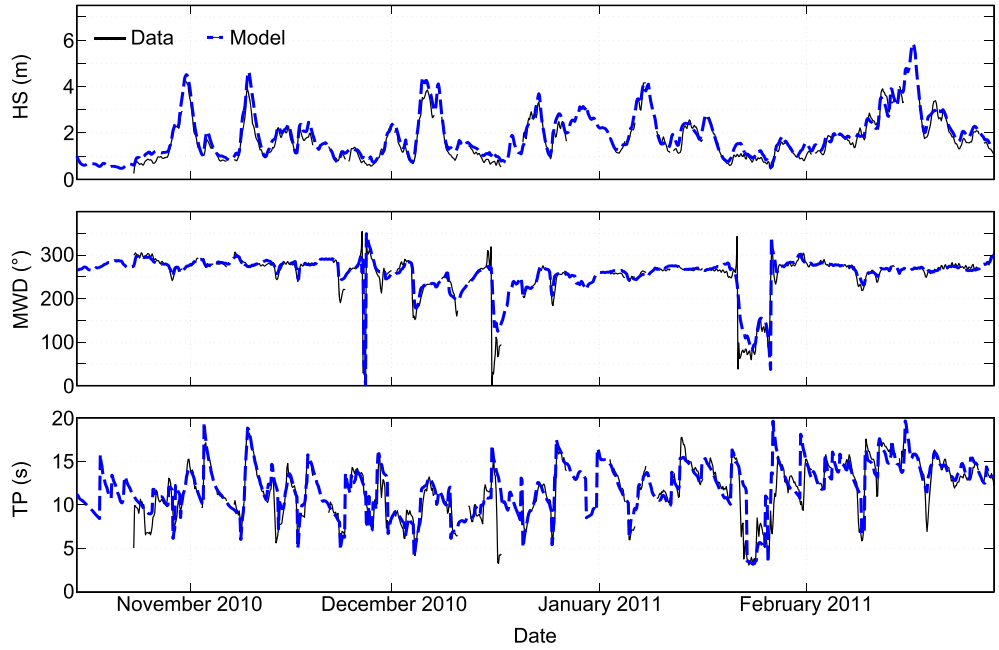

Figure 6. Comparisons between modeled (blue dashed line) and measured (black line and circles) mean wave parameters (HS, MWD, and TP) at the Lisbon buoy from October 2010 to March 2011.

work period, model outputs were also compared to wave data measured 100 km south and 250 km north of the study location and showed similar results for this period.

4.2. Waves at the Inlet

4.2.1. HS and TP

[23] The time series of elevation measured by the three pressure transducers were used to compute variance density spectra and the mean wave parameters HS and TP during the field work period in order to compare them with the model results (Figures 7–9). At each location and during each tidal cycle, the measured HS signal varied strongly in time, with the lower values (respectively higher) occurring at minimum (respectively maximum) water depth (Figure 7). This tide-modulated shape of HS is characteristic of the depth-induced breaking process and indicates that the instruments recorded waves which had already broken over the shallow bottom. For PT2 and PT3, HS dropped faster during the ebb phase of each tidal cycle than it rose during flood, whereas it evolved symmetrically at PT1. At PT1, PT2, and PT3, maximum HS were respectively 1.30, 0.16, and 0.39 m and occurred on 24 September when the oceanic tide and the offshore wave height were the highest.

[24] The peak period did not display such a large spatial variability as for HS, with mean values very similar for the three sensors (Figure 8). The time variation of TP was characterized by a strong shift between the first and the second tidal cycle, with values increasing from 10–15 s to 20–25 s. When HS was very low, values of TP were systematically exceeding (~30 s) the frequency range of gravity waves. For this reason, both measured and modeled TP were filtered out if HS were lower than 0.02 m.

[25] The modeled HS with *config.2* and *config.3* exhibited some significant differences (Figure 7). The parabolic shape of HS in *config.2* was rather symmetric for the three locations while it was asymmetric (negative skew) for the two locations in the inlet (PT2 and PT3) when the currents were included in the simulation (*config.3*). The amplitude of HS was almost always higher when the currents were not taken into account. The comparisons with the data clearly showed a better match for *config.3*, especially during the ebb stage at PT2 and PT3 when HS dropped quickly. The large bias observed between the data and the model during the last tidal cycle at PT3 was attributed to bathymetric changes that occurred during the campaign, particularly near the sand spit where PT3 was located, that were not taken into account in the model.

[26] Regarding the comparisons of TP, both model configurations matched well the data and captured the transition from the 12 s swell to the 20 s swell (Figure 8). The difference between *config.2* and *config.3* indicates that the currents had an impact on the modeled wave propagation. The statistical errors between measurements and model results for HS and TP are given in Table 2.

4.3. Spectral Analysis

[27] To get a better insight on wave energy variation in the inlet and model capabilities, time series of variance density (referred hereafter as energy) spectra at PT1 and PT2, computed from data and model outputs, were plotted and compared with each other (Figure 9). The main spectral characteristic deduced from the data was the presence of large amounts of energy not only at the offshore peak frequency f_p, but also at lower frequencies than f_p, corresponding to infragravity waves, and at harmonic frequencies, near $2f_p$ and $4f_p$. During the ebb stage, an abrupt decrease of energy was noticed at PT2 starting from the higher frequencies and generalizing to all frequencies in a short time, while the energy distribution at PT1 appeared to be less influenced by the tidal stages.

[28] The modeled spectral energy showed important differences depending on whether the current was taken into

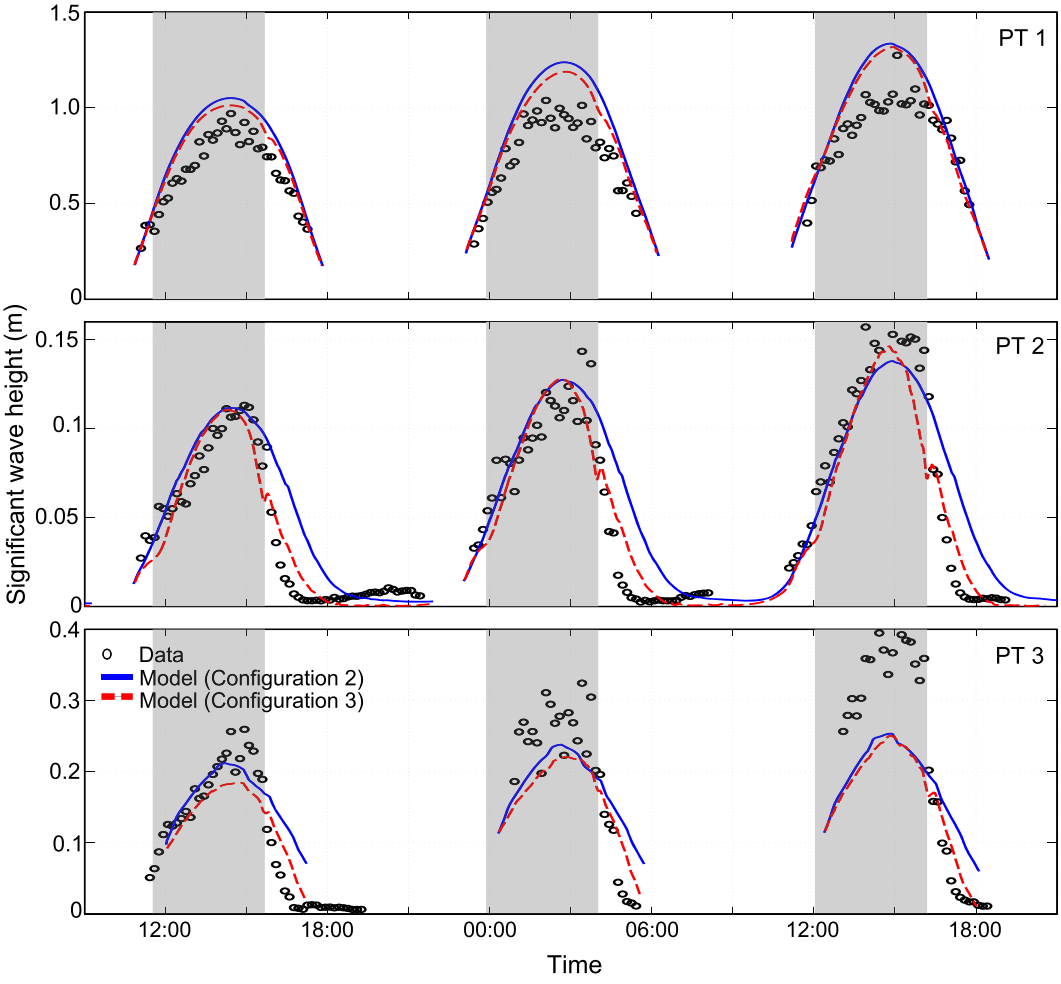

Figure 7. Comparisons between modeled and measured significant wave heights at (top) PT1, (middle) PT2, and (bottom) PT3 at the Albufeira Lagoon on 23–24 September 2010. The gray areas indicate flood tide when modeled currents flow toward the lagoon.

account in the wave propagation model (*config.3*) or not (*config.2*). For both locations, it appeared that the spectral energy was more diffused over the frequencies when current feedback was activated. In particular the energy patches at f_p, $2f_p$, and $4f_p$ were always less pronounced for *config.3*; and, in general, the spectral energy modeled with *config.3* had more similarities with the measured spectral energy. Also, at PT2, the energy decrease during the ebb tide occurred much sooner compared to *config.2*, which resembled much better the patterns in the data.

4.4. Water Level at the Inlet

[29] The water level measured by the pressure transducers was compared to the model results to assess the model performance in terms of prediction of the sea surface elevation (Figure 10). For the three tidal cycles, the maximum measured elevations at PT1—where the oceanic tide was not subjected to significant changes—were respectively 1.48, 1.41, and 1.61 m. Through the inlet (PT2 and PT3), the maximum elevations decreased on average by 10%. Moreover, the tidal signal was strongly distorted as it passed through the inlet and the flood duration became much shorter (~5 h) than the ebb duration (~7.5 h).

[30] The model results of *config.2* and *config.3* exhibited very minor differences (the mean bias and RMSE were smaller than 1 cm for the three locations), so only *config.2* was used for comparison with *config.1* in Figure 10. The comparisons between the model results displayed some significant differences: the elevation in *config.2* was always higher than in *config.1* (mean difference = 0.04 m), and the largest differences always occurred when the oceanic tide was near the mean sea level (maximum difference = 0.23 m). The comparison with the data showed that the model results of *config.2* reproduced the elevation more accurately, decreasing the mean RMSE by 40% (Table 3).

4.5. Velocity at the Inlet

[31] In order to validate the modeled velocity, the currents measured by ECM2 were compared to the model results (Figure 11). This data set was the only one which could be exploited. Indeed the measurements of the current profiles by the ADCP, located in the surf zone most of the time, were skewed because of the turbulence induced by the wave breaking process. Moreover ECM3 got buried during the first tidal cycle and its subsequent displacement resulted in a very heterogeneous set of data that was not usable. For a tidal cycle, on average, measured flood velocities lasted

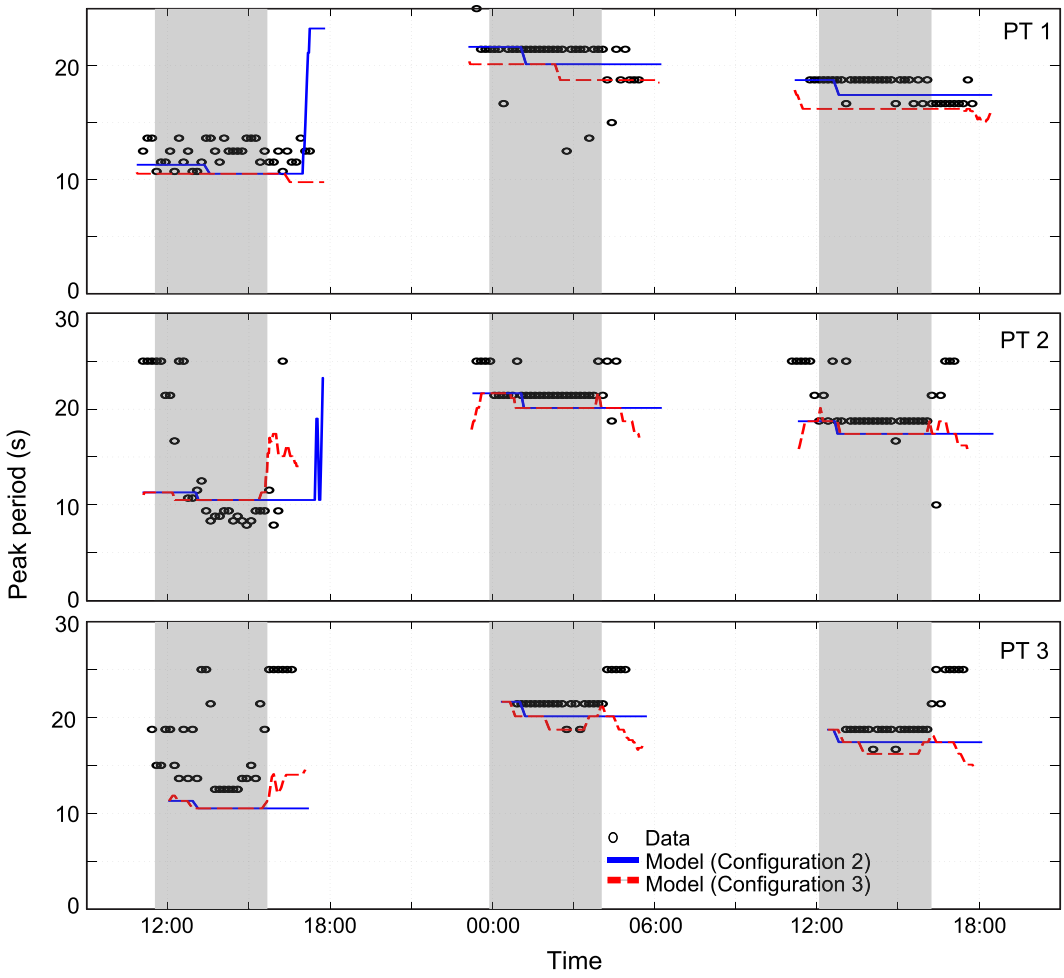

Figure 8. Comparisons between modeled and measured peak period at (top) PT1, (middle) PT2, and (bottom) PT3 at the Albufeira Lagoon on 23–24 September 2010. The gray areas indicate flood tide when modeled currents flow toward the lagoon.

4.3 h and exceeded 0.5 m s^{-1} during 60% of this duration, with a maximum of 1.4 m s^{-1}, while ebb velocities lasted 8.0 h and were almost always lower than 0.5 m s^{-1}. However, part of the ebb current was not measured when the sensor was dry and maximum ebb velocities remained unknown. In addition, ECM2 was located on the ramp of the flood-tidal delta, which receives flood currents but is sheltered from the ebb currents that are channelized around the flood-tidal delta [*Hayes*, 1979].

[32] The velocities simulated with the 2-DH modeling system were assumed to be reasonably comparable with the currents measured locally by ECM2 at 0.4 m above the bed. Indeed the large bed forms observed at low tide, the strong measured velocities, and the shallow depth provided a well-mixed environment where currents measured at this height were probably representative of velocities integrated over the water column. Comparisons between the data and the model outputs for *config.1* and *config.2* showed an RMSE of 0.10 m s^{-1} (SI = 21%) and 0.09 m s^{-1} (SI = 20%), respectively (Table 3).

[33] Significant low frequency fluctuations were observed in the velocity and elevation signals and a spectral analysis revealed that the associated energy was located in the infragravity band (0.004–0.04 Hz). The 1–5 min fluctuations of the velocity signal reached up to 50% of the filtered signal and were expected to have a significant impact on the sediment dynamics of the inlet. These low-frequency fluctuations need to be investigated in further detail and will be the subject of future study; they will not be discussed in this paper though.

5. Discussion

[34] Based on in situ data and local model outputs, the interactions between waves and currents appeared to be significant for the hydrodynamics of the inlet. The coupled wave-current modeling system was shown to perform well at Albufeira Lagoon in the presence of a complex tidal and wave forcing. The modeling system was used to investigate with more details the interactions between waves and currents as well as their impact on sediment dynamics. In order to verify if the physical processes observed in the data set do not depend on a particular wave climate and to avoid the interference between the variation in the incident forcing and the locally induced variability, an additional set of simulations was performed. These simulations were forced by a synthetic tide represented by the constituent M2 with an amplitude of 1 m (mean tidal amplitude) and yearly means of

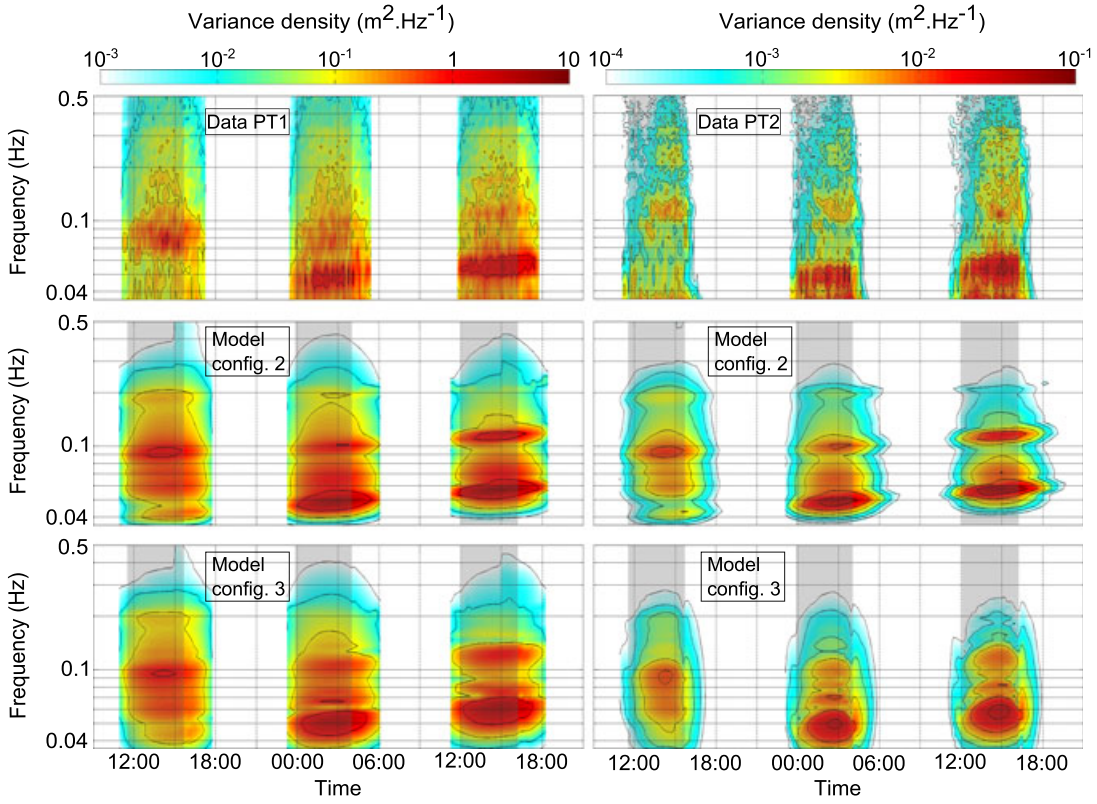

Figure 9. Time series of variance density spectra at (left column) PT1 and (right column) PT2 computed from the (top row) data and from the model with (middle row) *config.2* and (bottom row) *config.3* at the Albufeira Lagoon on 23–24 September 2010. The gray areas indicate flood tide when modeled currents flow toward the lagoon.

Table 2. Statistical Errors Between Data and Model Results for HS and TP [a]

	HS			TP		
	Bias (cm)	RMSE (cm)	SI (%)	Bias (s)	RMSE (s)	SI (%)
Configuration 2						
PT1	15.9	18.5	24.1	−0.4	2.1	12.4
PT2	0.9	2.3	40.9	−2.4	4.9	25.7
PT3	−1.7	7.9	40.1	−4.0	5.9	29.7
Configuration 3						
PT1	12.4	15.3	20.0	−1.6	2.2	13.2
PT2	−0.3	1.6	27.8	−2.2	5.0	26.3
PT3	−3.9	7.7	38.6	−4.3	5.7	28.4

[a]RSME: Root Mean Square Error; SI: Scatter Index.

HS (1.9 m), TP (10.5 s), and MWD (312°). Model outputs were stored over the computational grids during one tidal cycle and were used to compute spatial representations of several forcing terms at two different time steps, representative of flood and ebb situations. These representative time steps were chosen so that flood and ebb flows were of similar intensity and strong enough to have an impact on the wavefield. These maps are used along the discussion to support the analysis based on the local data presented in section 4.

5.1. Wave-Induced Effects on the Hydrodynamics of the Inlet

[35] When waves break in the surf zone, they release a large fraction of their energy and they transfer their momentum to the water column. This process induces a gradient of the water surface to balance the onshore component of the momentum flux, resulting in a higher water level along the shoreline (wave-induced setup) and at the inlet. *Hench and Luettich* [2003] analyzed the momentum balance in both an idealized and a natural inlet without waves and showed that near maximum flood and maximum ebb, the along-stream momentum balance was dominated by advection, pressure gradient, and bottom friction. *Olabarrieta et al.* [2011] corroborated these results at Willapa Bay, where they applied a fully coupled modeling system. They also showed that when the wave forces were present, the pressure gradient and the bottom friction terms were greatly affected, inducing a significant setup of the water level inside the estuary. The effect of the waves on the water level at each instrument location was computed as the difference between the elevations simulated with *config.1* and *config.2* (Figure 10). For each location, this difference (hereafter referred to as "setup") was characterized by a strong tidal modulation. At PT1, the minimum setups were obtained during high tides, as the sensor was near the wave breaking point, while the maximum values occurred at the lowest measured water depths, when the instrument position coincided with the shoreline position. At PT2 and PT3, the setup signal was out-of-phase with the local elevation signal and maximum values occurred when the oceanic tide was near mean sea level. In order to understand the effect of the waves on the water level inside the lagoon, the magnitude and directions of the dominant terms (barotropic pressure, bottom

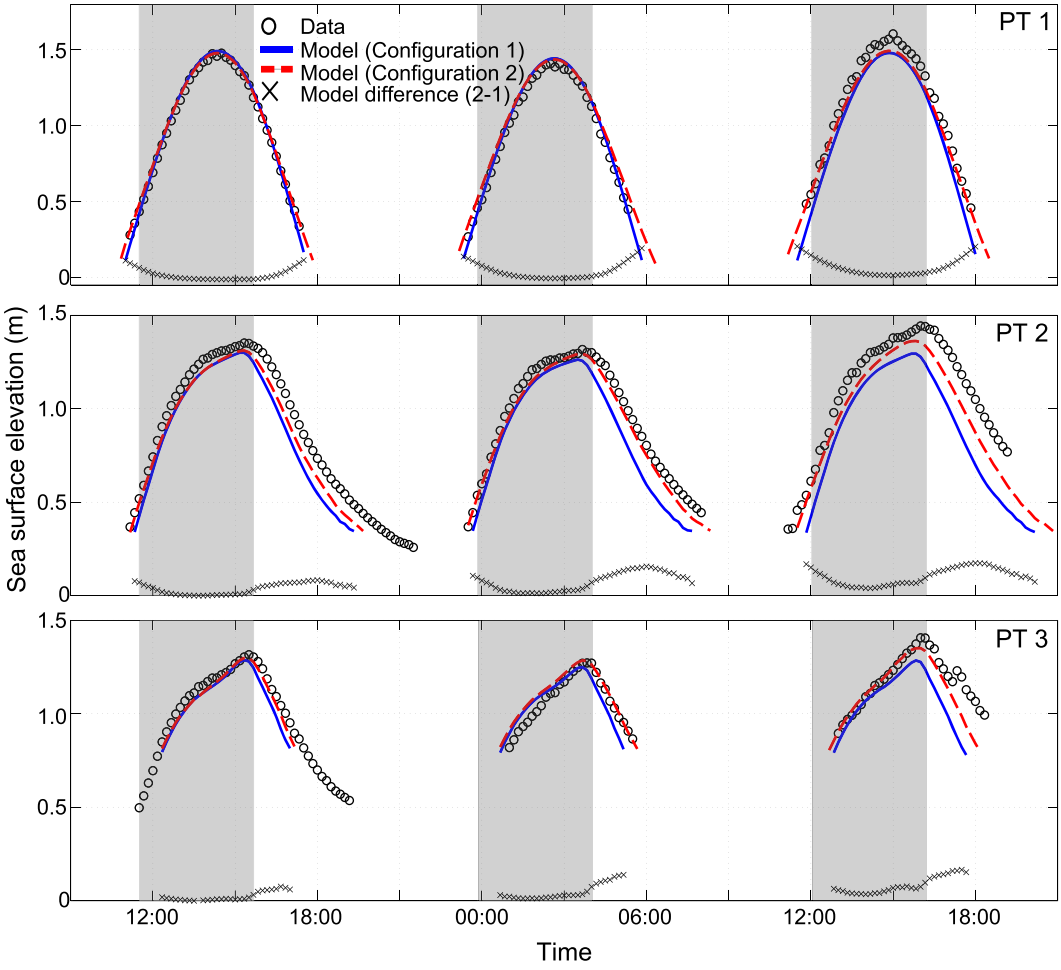

Figure 10. Comparisons between modeled and measured sea surface elevation at (top) PT1, (middle) PT2, and (bottom) PT3 at Albufeira lagoon on 23–24 September 2010. The gray areas indicate flood tide when modeled currents flow toward the lagoon.

Table 3. Statistical Errors Between Data and Model Results for Elevation And Current Velocity[a]

	Elevation		Velocity	
	Bias (cm)	RMSE (cm)	Bias (cm s^{-1})	RMSE (cm s^{-1})
Configuration 1				
PT1	−2.5	7.2	NA	NA
PT2	−14.4	16.7	2.8	9.6
PT3	−6.2	10.9	NA	NA
Configuration 2				
PT1	1.3	5.1	NA	NA
PT2	−7.6	8.9	3.6	9.2
PT3	−1.9	7.2	NA	NA

[a]RMSE = Root Mean Square Error.

friction, wave radiation stress gradients, and advection) in the momentum equations (equations (12) and (13)) were computed for the representative flood and ebb situations (Figure 12). The balance between barotropic pressure, bottom friction, and advection mentioned by *Hench and Luettich* [2003] was significantly affected by the contribution of the wave radiation stress term, corroborating the results of *Olabarrieta et al*. [2011]. Indeed, for both situations, the wave radiation stress term oriented toward the lagoon was of the same order of magnitude as the other terms and thus had an important impact on the overall hydrodynamics, the main impact being a wave-induced setup along the shoreline and inside the lagoon. During ebb, when the ocean water level is near mean sea level, the waves break directly over the ebb shoal leading to stronger values of the wave radiation stress term than during flood when the water level is higher and waves are subjected to less intense breaking. This difference in intensity of the wave radiation stress term explains why the higher modeled setup values at PT2 and PT3 were found when oceanic water level was near mean sea level. The friction term in the inlet was generally higher during ebb than during flood and reached very large values at the end of the ebb (not shown here) attesting that sediment transport in such inlet is clearly ebb dominated during low-to-moderate wave energy conditions, as shown by *Bertin et al*. [2009] at a similar wave-dominated inlet. It is worth noting that values of the different terms of the momentum equations reached almost 0.1 m s^{-2}, which is several orders of magnitude higher than in the case of Willapa Bay [*Olabarrieta et al*., 2011] and other large systems [*Hench and Luettich*, 2003]. This difference supports the fact that very shallow wave-dominated inlets (~1 m deep) are extremely dynamic and thus represent a great challenge for measurements collections and model applications.

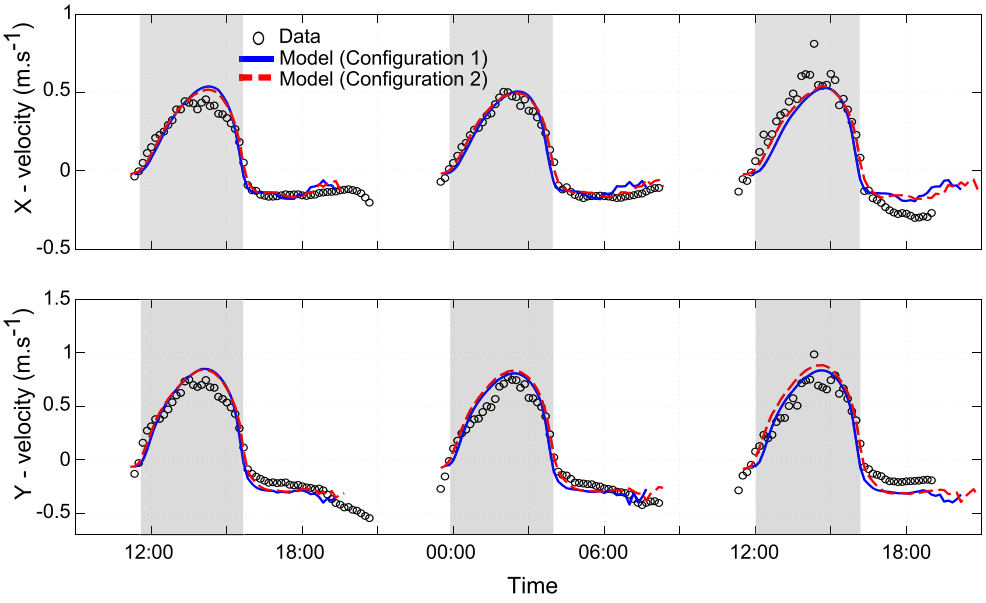

Figure 11. Comparisons between modeled and measured (top panel) cross-shore and (bottom panel) longshore current velocities at ECM2 at Albufeira lagoon on 23–24 September 2010, on the top panel (respectively bottom panel). The gray areas indicate flood tide when modeled currents flow toward the lagoon.

[36] For PT1, PT2, and PT3, the maximum setup occurred during the third tidal cycle, when offshore wave height was maximal (1.72 m), reaching the respective values of 0.23, 0.18, and 0.19 m. On average, the maximum setup represented 11% of the offshore wave height (Table 4), corroborating the 10–14% range estimated by *Nguyen et al*. [2007] for storm-induced setup at narrow and shallow inlet mouth. Finally, other simulations carried out with a shore-normal and deeper inlet morphology (not shown here) produced lower maximum setups (7% of the offshore wave height on average), which corroborated the findings of *Malhadas et al*. [2009] who used model simulations to show that the wave-induced setup in an inlet was lower for the deeper morphology of their synthetic tidal inlet.

[37] The impact of the waves on the currents was almost negligible at ECM2 as shown by the difference between the currents modeled with *config. 1* and *config. 2* (Figure 11). However, spatial plots of the current magnitude difference for these two configurations at key phases of the tide (not shown) revealed that the wave-induced currents could reach up to 1 m s^{-1} near the ebb shoal during ebb and 0.5 m s^{-1} along the beach as longshore drift. These results also confirmed that the wave-induced currents were very weak in the channel for the considered offshore wave climate.

5.2. Impact of Currents on Wave Propagation

[38] Among the effects of currents on the incident wavefield, summarized for instance by *Wolf and Prandle* [1999], the current-induced refraction, the Doppler shift of wave frequency, and the wave blocking (in the case of countercurrents) are all represented in the formulation of wave action conservation in phase-averaged wave models, with some limitations though (see section 6). Several authors tested the skills of coupled wave-current modeling systems by comparing model results either with laboratory measurements [*Ris and Holthuijsen*, 1996; *Rusu et al*., 2011] or with field data [*Westhuysen*, 2012]. In general, the models were able to reproduce the main effects of the ambient current on the wavefield, although some inaccuracies remained, particularly in the presence of strong opposing currents [*Ris and Holthuijsen*, 1996; *Van Dongeren et al*., 2010]. In order to analyze the ability of our modeling system to reproduce the effects of the currents on the incident wavefield, model results obtained with *config.2* and *config.3* were compared with field data (Figure 7). The HS signal was better reproduced with *config.3* particularly during the ebb tide. The larger differences between the two configurations were observed in the inlet (PT2 and PT3) where the waves were subjected to opposing currents as they passed through the inlet: for each tidal cycle, the modeled HS was much more asymmetric if the currents were taken into account in the wave model, particularly during the ebb tide when the HS experienced a fast drop.

[39] Several authors reported that wave propagation could be blocked in the presence of strong countercurrents, based on physical and numerical modeling results [*Lai et al*., 1989; *Chawla and Kirby*, 2002]. Perhaps due to the difficulty of installing instruments in such dynamic environments, in situ measurements of wave-blocking conditions have been very rarely published to this day. *Ris and Holthuijsen* [1996] proposed that wave heights propagating over strong opposing, partially blocking currents were often overestimated due to insufficient steepness dissipation. *Westhuysen* [2012] implemented an enhanced dissipation term for waves on negative current gradients to counteract this overestimation. The model results presented in this study benefit from this recent development, which improved the comparison of HS in the inlet during ebb. In order to investigate the effect of following and countercurrents on the wavefield and determine if the strong attenuation of HS during the ebb tide was the result of steepness dissipation on negative current gradients and wave blocking mechanism, numerical simulations were carried out using the synthetic forcing. For the flood and ebb situations, the current velocity $\vec{U}$, the intrinsic group velocity

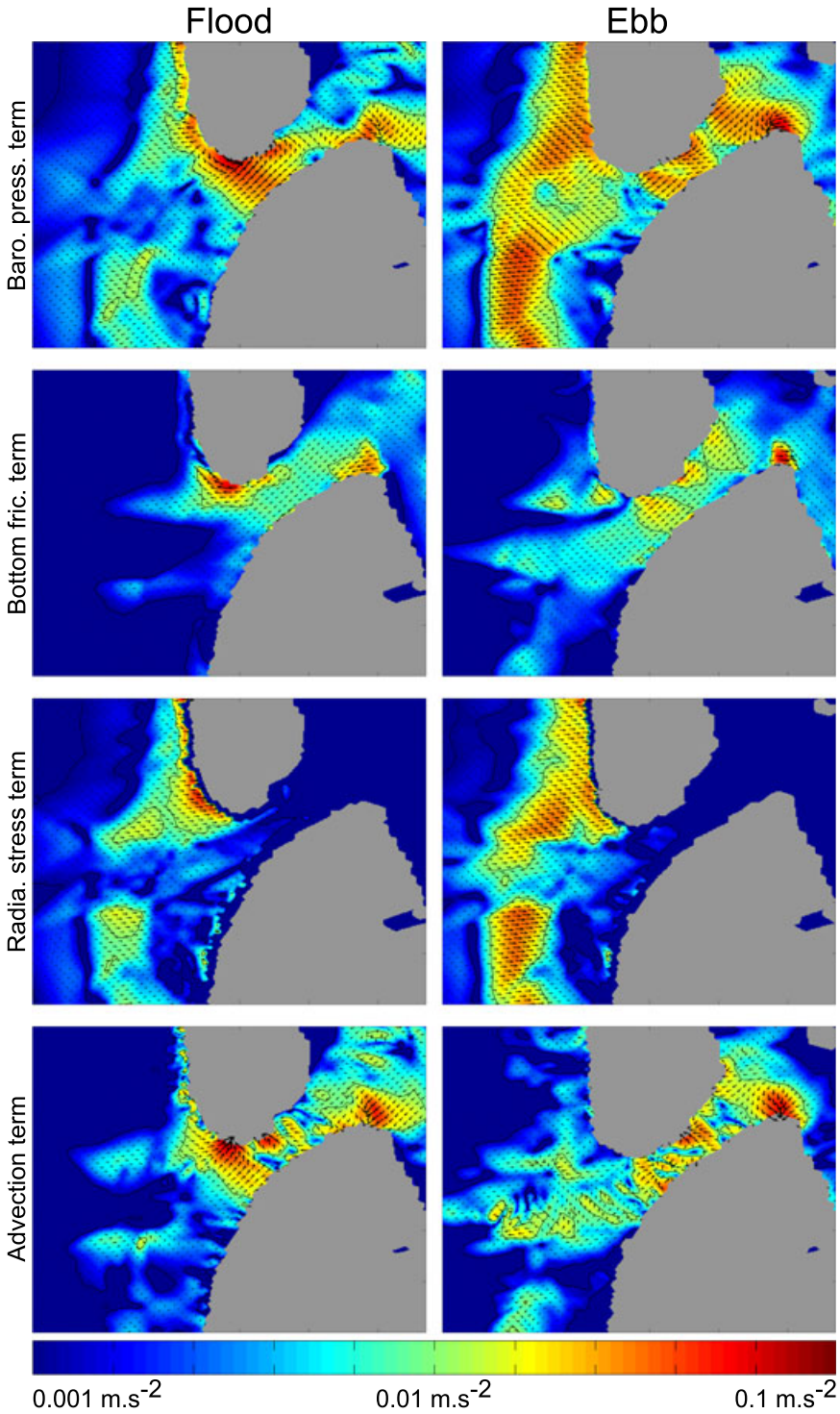

Figure 12. Dominant terms of the momentum equations: (first row) barotropic pressure term, (second row) bottom friction term, (third row) wave radiation stress term, and (fourth row) advection term for (left column) flood and (right column) ebb. The colors represent the magnitude of each term. The vectors represent the direction of each term.

$\overrightarrow{Cg} + \overrightarrow{U}$, the velocity gradient $\frac{\partial U_s}{\partial s}$, where U_s is the current velocity component in the direction of wave propagation and s is the coordinate in the wave direction, HS, and the relative HS difference $((HS_{current} - HS_{no\_current})/HS_{current})$ were computed (Figure 13). During flood, the incident waves were refracted by the currents at the entrance of the inlet and the wave action focused on the edge of the main current as shown by the increase in HS (up to 10%) on the margins of the main channel and the decrease in HS (up to 10%) along the channel. The current gradients encountered by the incident waves were mainly positive and thus did not impact on the whitecapping dissipation process. Large HS differences

Table 4. Offshore Significant Wave Height and Setup[a]

Tidal cycle	Offshore HS (m)	Setup					
		PT1		PT2		PT3	
		Abs. (m)	Rel. (%)	Abs. (m)	Rel. (%)	Abs. (m)	Rel. (%)
Tide1	1.17	0.15	12.8	0.22	15.0	0.23	13.4
Tide2	1.47	0.09	7.7	0.16	10.9	0.18	10.5
Tide3	1.72	0.10	8.5	0.16	10.9	0.18	11.0

[a]Relative setup is normalized by offshore significant wave height.

(up to 30%) appeared after the wave passed the inlet and can be explained by current-induced refraction. However, these differences concern only very small waves and their impact on the overall inlet dynamics was very limited since most of the waves' energy had already been dissipated after propagation through the channel. During ebb, currents were strong enough (up to 1.5 m s^{-1}) to cancel the intrinsic group velocity in the inlet. In addition, the negative current gradients at the entrance of the inlet reached large values (up to 0.03 s^{-1}), strongly increasing wave steepness responsible for enhanced whitecapping dissipation, as proposed by *Westhuysen* [2012]. The relative difference of HS showed that the waves were refracted by the ebb-jet current at the entrance of the inlet where HS of *config.3* was locally 20% larger when currents were included in the wave model. As the waves traveled along the inlet, their HS quickly decreased and became much lower (up to 50%) than in the situation without currents. It is assumed that the strong HS attenuation during the ebb, as observed in the data, resulted from current-induced breaking dissipation at the entrance of the inlet and from the blocking of the wave energy when the current approached the absolute wave group velocity.

[40] The difference in current magnitudes for *config.2* and *config.3* (not shown here) indicated that the current-induced modification of the wavefield near the inlet had a minor impact on the currents in the channel (less than 0.05 m s^{-1}) but could reach up to 0.5 m s^{-1} at the entrance of the inlet where the ebb jet induced an increase of HS and thus a more energetic breaking.

5.3. Consequences for Sediment Dynamics

[41] Wave-dominated tidal inlets can be subjected to considerable morphological changes in a very short time. Under certain conditions, they may naturally close and thus prevent water exchange with the ocean, leading to a rapid modification of water dynamics and chemical composition that eventually affect the ecosystem and the local populations. *Ranasinghe and Pattiaratchi* [1999] studied an ephemeral inlet in Australia and suggested that inlet closure was mainly induced by onshore sediment transport under persistent swell conditions, typical of summer periods. However, inlet closures may occur under stormy winter conditions in other parts of the world [*Winton and Mehta*, 1981; *Freitas and Andrade*, 1994; *Bertin et al*., 2009; *Nahon et al*. 2012b]. Based on the results of a morphodynamic modeling system, *Bertin et al*. [2009] attributed inlet closure to the following processes: (1) a bulldozer effect due to the onshore component of radiation stress gradients, (2) lateral barotropic pressure gradients accelerating longshore transport, (3) wave refraction over the ebb-tidal delta shoal, and (4) increased water levels reducing ebb dominance in the inlet mouth. Nevertheless, these authors underestimated the shoaling of the inlets under energetic wave conditions. These findings indicate that further investigation is needed to accurately predict inlet dynamics with process-based modeling systems. In order to investigate the effects of the current-induced wave transformation on sediment transport, model outputs of *config.2* and *config.3* using the synthetic forcing were used. For each configuration, the Soulsby-Van Rijn formulation [*Soulsby*, 1997] was used to compute the sediment fluxes induced by currents and waves over the domain. Then the net total transport was obtained by integrating the sediments fluxes over a tidal cycle. The net sediment fluxes displayed similar patterns for both configurations (shown with vectors in Figure 14 for *config.3*). Along the inlet throat, the transport was oriented seaward with stronger values at the entrance of the inlet, where the ebb jet formed during ebb tide, and in the narrowest part of the inlet where the currents were accelerated. Transport toward the lagoon occurred mostly over the ebb shoal and on the channel margins, which remained dry during most of the ebb tide. After integrating the net transport over channel sections, the sediment balance showed to be highly dependent on the chosen section. In the narrowest part of the channel, the transport was clearly ebb dominated (Figure 14a) while it was almost in balance at the channel entrance (Figure 14b). The net transport difference between *config.3* and *config.2* (colors in Figure 14) was larger at the entrance of the inlet with lower values (up to −60%) in the deeper ebb-dominated part and with both higher (up to 40%) and lower values over the ebb shoals which are flood dominated. These differences were directly correlated to the impact of the currents on the wavefield. Indeed, ebb currents induced enhanced dissipation and partial blocking of the incident waves, decreasing their orbital velocity and thus their sediment stirring effect. During flood, wave energy focused on either sides of the currents, increasing their height and orbital velocity on the exterior part of the ebb shoals and decreasing their height and orbital velocity on the interior part of the shoals and in the channel. The transport differences rapidly decreased toward the lagoon where the wave energy was too weak to have a significant impact on the sediment movements. The uncertain balance between flood- and ebb-dominated transport at the entrance of the inlet and the large difference induced by the wavefield, whether it is modified by the current or not, support the major impact of wave-current interactions on the morphological evolution of tidal inlet. Based on these findings, the impact of the currents on the incident wavefield hinders the seaward sediment

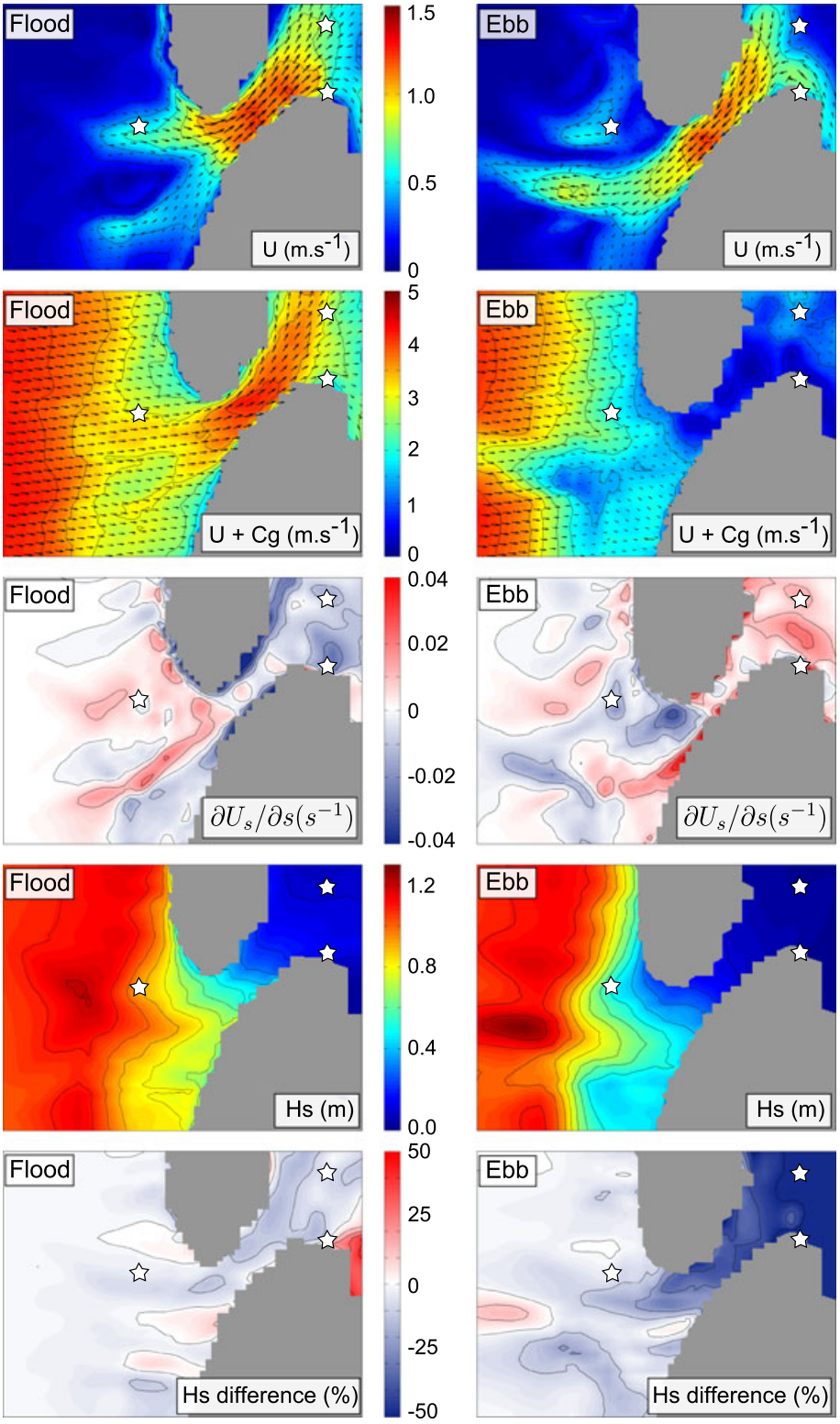

Figure 13. (first row) Currents, (second row) intrinsic wave group velocity, (third row) gradient along the wave propagation direction of the velocity component in the direction of the wave direction, (fourth row) significant wave height, and (fifth row) relative difference between significant wave height computed with *config.3* and *config.2* normalized by the wave height computed with config.3, during (left column) flood and (right column) ebb.

transport and may even tip the scale in favor to flood dominance, in some part of the inlet. This process is believed to contribute to the accretion of wave-dominated inlet during energetic conditions and justifies the importance of including the current effects on wave propagation in morphodynamic modeling systems for the study of similar environments.

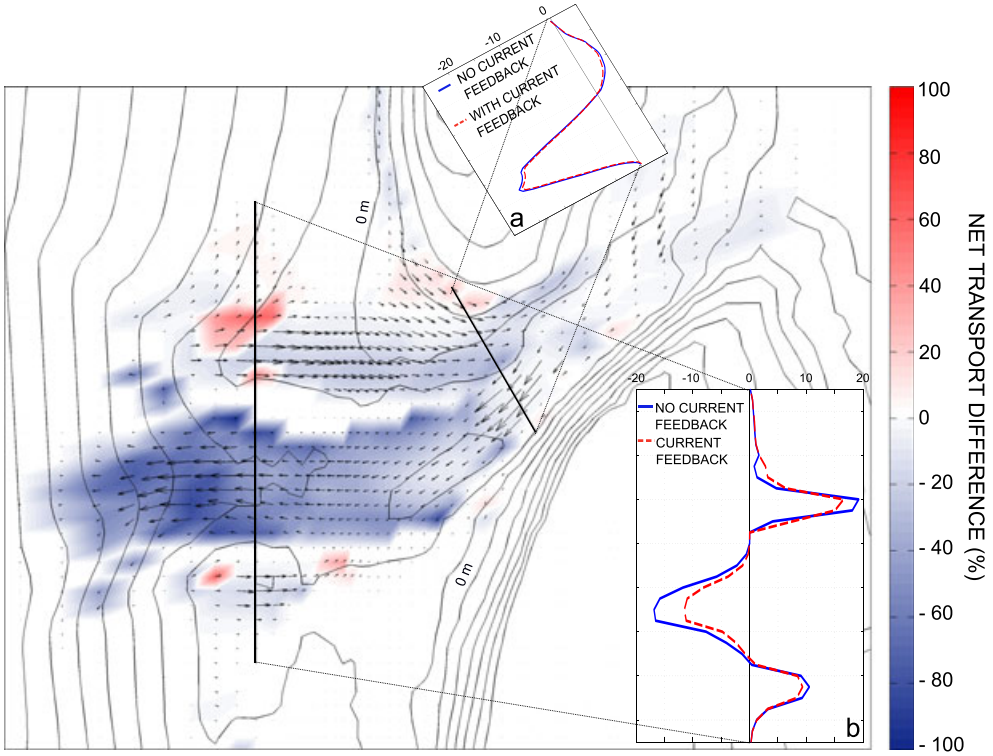

Figure 14. Net sediment transport computed with *config.3* (vectors) and relative difference between the net transport computed with *config.3* and *config.2* normalized by the net transport computed with *config.3* (colors). Streamwise component of the net sediment transport computed with model results of *config.2* (solid blue line) and *config.3* (red dashed line) along two sections: (a) one in the inlet and the (b) other at the entrance of the inlet.

5.4. Limitations of This Study and Perspectives

[42] The modeling system presented in this study is under development and several aspects have not been implemented yet, whose potential impacts on the present results are discussed here.

5.5. Nonlinear Effects

[43] As waves encounter strong opposing currents, they become increasingly nonlinear, making the linear wave balance equation (2) and the linear kinematic expressions (3)–(5) inadequate. *Chawla and Kirby* [2002] showed that nonlinear amplitude dispersion affected significantly their results near the blocking point. They used a third-order Stokes dispersion relation and compared their results with the same model using a linear dispersion relation. The former performed much better and was more accurate to predict the position of the blocking point along the flume. The modeling system presented in this study used the SWAN wave model which does not provide the possibility to use different formulations for the dispersion relation. The authors are aware of this limitation; this is why they settled for describing the different physical processes in a qualitative manner as much as possible. Therefore, potential improvements for this modeling system could be the implementation of a higher order dispersion relation in the wave model to take into account the effect of amplitude dispersion near the blocking point. Another alternative to accurately predict the wave propagation in a strongly inhomogeneous media is given by *Toledo et al*. [2012] who derived a new form of the wave action equations based on the extended mild-slope equation. Their sophisticated formulation resolves higher-order bottom and current effects and is therefore adapted to shallow inlet applications.

5.6. Current-Induced Wave Reflection

[44] *Smith* [1975] showed that away from the blocking region, the wavefield consists of an incident wave and a much shorter reflected wave. *Suastika et al*. [2000] observed reflected waves by blocking currents in laboratory experiments. In SWAN, wave components are not propagated into the opposing current once the blocking point is reached for that component. So, at that point, the variance density becomes zero at that component's spectral bin. In order to model accurately the wavefield in an inlet during ebb when tidal currents are likely to block the incident waves, the wave model should simulate wave propagation in all directions. Taking into account this effect would enable to reproduce more accurately the wave spectra in the inlet.

5.7. Wave Energy Dissipation Induced by Countercurrents

[45] Several studies based on SWAN results showed that the modeled wave height was overestimated when waves encountered strong opposing currents [*Ris and Holthuijsen*, 1996; *Westhuysen*, 2012]. The present study benefitted from the recent improvements of *Westhuysen* [2012] to simulate enhanced wave energy dissipation on negative countercurrents.

It is worth noting that setting a large calibration coefficient was necessary (5 here against the 0–3 range of *Westhuysen* [2012]) to observe significant differences in the model results, and yet the results of our study suggested that the wave model still overestimates wave heights during ebb. Given the limitation of our data set and the complexity of the study site, the calibration of the enhanced dissipation term was mostly qualitative. The objectives of the present study were to highlight physical processes induced by wave-current interactions much more than calibrating and validating a new empirical formulation. The results of our study confirmed the fact that the wave model overestimated wave height during ebb. This raises the need to pursue experimental research on enhanced wave energy dissipation in opposing currents.

6. Conclusions

[46] This study investigated the interactions between tidal currents and incident waves at a shallow tidal inlet. The twofold objective of this work was to improve our understanding of the physical processes driving shallow inlet hydrodynamics and to discuss the impacts of the wave-current interactions on the sediment transport in the inlet. A numerical modeling system was implemented to perform coupled wave-current simulations in the very dynamic barrier beach-inlet-lagoon system of Albufeira in Portugal. The comparisons of the model results with in situ hydrodynamic data were very satisfactory and improved when waves and wave-current interactions were taken into account. In order to highlight the effects of the interactions between waves and currents on the overall hydrodynamics, a set of simulations was performed with a synthetic forcing representative of yearly mean conditions. The analysis of the results revealed that

[47] 1. the wave-induced setup in the lagoon comprised between 7% and 12% of the offshore significant wave height, depending on the inlet morphology: the shallower the inlet, the higher the setup;

[48] 2. during ebb, the wave height increased at the entrance of the inlet (up to 20%) and was attenuated through the inlet (up to 40%). The main responsible mechanisms are proposed to be wave blocking and current-induced wave breaking dissipation;

[49] 3. during flood, the currents had less impact on the waves: current-induced refraction decreased wave height along the inlet throat (up to 10%) and increased wave height on the exterior part of the ebb shoals;

[50] 4. the effects of the currents on the wavefield significantly attenuated seaward residual sediment transport.

[51] The authors propose that this last finding plays a significant role in the sediment transport balance of the inlet during stormy conditions. They suggest that the inclusion of current feedback on waves in a coupled wave-current transport modeling system is required for accurate morphodynamic predictions.

[52] **Acknowledgments.** This work was part of two projects funded by the Portuguese Foundation for Science and Technology (FCT): 3D-MOWADI (PTDC/ECM/103801/2008) and G-CAST (GRID/GRI/81733/2006). It was also part of the project ANR JC DYNAMO (agreement ANR-12-JS06-00008-01). The third author was funded by an FCT post-doctoral research grant (SFRH/BPD/67041/2009). The wave models (WAVEWATCH III and SWAN) and the circulation model SELFE were provided by the U.S. National Oceanic and Atmospheric Administration, the Delft University of Technology, and the Center for Coastal Margin Observation and Prediction, respectively. André Van der Westhuysen is acknowledged for sharing his recent model developments and for his constructive comments. Topographic and hydrodynamic data were obtained, thanks to the combined efforts of many individuals from the Faculty of Science of the University of Lisbon, the National Laboratory of Civil Engineering, and the University of Algarve. The wave data were provided by the Lisbon harbor. The time series of sea surface elevation at Cascais were provided by the Portuguese Geographic Institute.

References

Battjes, J.A., (1972), Radiation stresses in short-crested waves, *J. Mar. Res.*, *30* (1), 56–64.

Battjes, J. A. (1975), Modelling of turbulence in the surf zone, in *Proceedings of International Symposium on Modelling Techniques*, San Francisco, 2, 1050–1062, ASCE.

Bertin, X., A.B. Fortunato, and A. Oliveira (2009), A modeling-based analysis of processes driving wave-dominated inlets, *Cont. Shelf Res.*, *29* (5–6), 819–834, doi:10.1016/j.csr.2008.12.019.

Bertin, X., N. Bruneau, J.F. Breilh, A.B Fortunato, and M. Karpytchev (2012), Importance of wave age and resonance in storm surges: The case Xynthia, *Bay of Biscay. Ocean Modell.*, *42*, 16–30, doi:10.1016/j.ocemod.2011.11.001.

Booij, N., R. Ris, and L. Holthuijsen (1999), A third-generation wave model for coastal regions. 1. Model description and validation. *J. Geophys. Res.*, *104* (C7), 649–666.

Bosnic, I., J. Cascalho, R. Taborda, M. Ribeiro, A. Oliveira, A. Rodrigues, and C. Lira (2011), Textural Characterization of the Beach Active Layer, *J. Coast. Res.*, *SI 64* (Proceedings of the 11th International Coastal Symposium), Szczecin, Poland, ISBN 0749-0208.

Bretherton, F.P., and C.J.R. Garrett (1969), Wavetrains in inhomogeneous moving media, *Proc. Roy. Soc. A*, *302*, 529–554.

Brown, E. I. (1928), Inlets on sandy coasts, in *Proceedings of the American Society of Civil Engineers*, Vol. 54, Part I, pp 505–523.

Bruneau, N., A.B. Fortunato, G. Dodet, P. Freire, A. Oliveira, and X. Bertin (2011), Future evolution of a tidal inlet due to changes in wave climate, sea level and lagoon morphology (Óbidos Lagoon, Portugal). *Cont. Shelf Res.*, *31* (18), 1915–1930, doi: 10.1016/j.csr.2011.09.001.

Bruun, P. (1966), Tidal inlets and littoral drift: V. 2, *Universitesforlaget*, Oslo, 193 p.

Cayocca, F. (2001), Long-term morphological modeling of a tidal inlet: The Arcachon Basin, France, *Coastal Eng.*, *42* (2), 115–142.

Chawla, A., and J.T. Kirby (2002), Monochromatic and random wave breaking at blocking points, *J. Geophys. Res.*, *107* (C7), 3067, 4-1– 4–19.

Costa, M., R. Silva, and J. Vitorino (2001), Contribuição para o estudo do clima de agitação marítima na costa Portuguesa, in *Proceedings*, *II Jornadas Portuguesas de Engenharia Costeira e Portuária*, Sines, Portugal.

Davies, J. L. (1964), A morphogenic approach to world shorelines, *Zeitschrift für Geomorphologie*, *8*, 127–142.

Dee, D.P., Uppala, S.M., Simmons, A.J., Berrisford, P., Poli, P., Kobayashi, S., Andrae, U., (. . .), Vitart, F. (2011), The ERA-Interim reanalysis: Configuration and performance of the data assimilation system, *Q. J. R. Meteorolog. Soc.*, *137* (656), 553–597. doi: 10.1002/qj.828

Dodet, G., X. Bertin, and R. Taborda (2010), Wave climate variability in the North-East Atlantic Ocean over the last six decades, *Ocean Modell.*, *31*, 120–131, doi:10.1016/j.ocemod.2009.10.010.

Van Dongeren, A., A. Westhuysen, J. Groeneweg, G. Vledder, J. Lansen, A. Smale, C. Gautier, H. Peters, and I. Wenneker (2010), Spectral wave modelling in tidal inlet seas: Results from the SBW Wadden Sea Project, in *Proceedings of the International Conference on Coastal Engineering*, No 32, Shangai.

Elias, E. P. L., J. Cleveringa, M. C. Buijsman, Roelvink, J.A., and M.J.F. Stive (2006), Field and model data analysis of sand transport patterns in Texel Tidal inlet (the Netherlands), *Coastal Eng.*, *53*, 505–529, doi:10.1016/j.coastaleng.2005.11.006.

Freitas, M.C. (1995), A laguna de Albufeira (Peninsula de Setubal): Sedimentologia, morfologia e morfodinamica, PhD thesis, Dep. of Geol., Univ. of Lisbon, Lisbon, Portugal.

Freitas, M.C., and C. Andrade (1994), Tidal inlet evolution and hydraulic characteristics at Albufeira lagoon, in *Proc. LITTORAL*, *94*, 257–271.

Freitas, M.C., and T. Ferreira (2004), Lagoa de Albufeira. Geologia. Instituto da Conservação da Natureza/Centro de Zonas Húmidas.

Guedes Soares, C., and H. de Pablo (2006), Experimental study of the transformation of wave spectra by a uniform current, *Ocean Eng.*, *33*(3–4), 293–310, doi:10.1016/j.oceaneng.2005.05.005.

Hayes, M.O. (1975), Morphology and sand accumulations in estuaries, in Estuarine Research, vol. *2*., edited by Cronin, L.E., pp. 3–22, Academic Press, New York.

Hayes, M.O. (1979), Barrier Island morphology as a function of tidal and wave regime, in Barrier Island, edited by Leatherman, pp. 1–28, Academic Press, New York.

Hench, J. L. and A. Luettich Jr. (2003), Transient tidal circulation and momentum balances at a shallow inlet, *J. Phys. Oceanogr.*, *33*, 913–932, doi:10.1175/1520-0485(2003)33 < 913:TTCAMB > 2.0.CO;2.

Huang, N.E., D.T. Chen, C.C. Tung, and J.R. Smith (1972), Interactions between steady non-uniform currents and gravity waves with applications for current measurements. *J. Phys. Ocenogr.*, *2*, 420–431.

Keulegan, G. H. (1967), Tidal flow in entrances water-level fluctuations of basins in communications with seas, Technical Bulletin No. 14, Committee on Tidal Hydraulics, U.S. Army Engineer Waterways Experiment Station, Vicksburg, MS.

Lai, R.J., S.R. Long, and N.E. Huang (1989), Laboratory studies of wave–current interaction: Kinematics of the strong interaction. *J. Geophys. Res.*, *94* (16), 201–16,214.

Longuet-Higgins, M.S., and R.W. Stewart (1964), Radiation stresses in water waves: A physical discussion with applications, *Deep Sea Res.*, *11*, 529–562.

Malhadas, M. S., P. C. Leitao, A. Silva, and R. Neves (2009), Effect of coastal waves on sea level in Óbidos Lagoon, Portugal, *Cont. Shelf Res.*, *19* (9), 1240–1250, doi:10.1016/j.csr.2009.02.007.

Mehta, A.J., and E. Özsöy (1978), Inlet hydraulics, in Stability of Tidal Inlets: Theory and Engineering, edited by Bruun, P., pp. 83–161, Elsevier Scientific Publishing Co., Amsterdam, The Netherlands.

Mota Oliveira, I. B. (1970), Natural flushing ability in tidal inlets, in *Proceedings of the 12th Coastal Engineering Conference*, ASCE, 1827–1845.

Nahon, A., X. Bertin, A.B. Fortunato, and A. Oliveira (2012a), Process-based 2DH morphodynamic modeling of tidal inlets: A comparison with empirical classifications and theories, *Mar. Geol.*, *1–11*, 291–294, doi:10.1016/j.margeo.2011.10.001.

Nahon, A., P. Freire, A.R. Pires, G. Dodet, X. Bertin, M.C. Freitas, A.B. Fortunato, and C. Andrade (2012b), Morphodynamique d'une embouchure tidale artificielle éphémère : la lagune d'Albufeira, Portugal, paper presented at XIIèmes Journées Nationales Génie Côtier – Génie Civil, Cherbourg, France. DOI: 10.5150/jngcgc.2012.038-N.

Nguyen, X. T., H. Tanaka, and H. Nagabayashi (2007), Wave set-up at river and inlet entrances due to an extreme event, in *Proceedings of International Conference on Violent Flow* 2007 [CD-ROM].

Nielsen, P. (1992), *Coastal Bottom Boundary Layers and Sediment Transport*, World Scientific.

O'Brien, M. P. (1931), Estuary tidal prisms related to entrance areas, *Civil Eng.*, *1* (8), 738–739.

O'Brien, M. P. (1969), Equilibrium flow areas of inlets on sandy coasts, *J. Waterways Harbors Div.*, American Society of Civil Engineers, (WWI), 43–52.

Olabarrieta, M., J. C. Warner and N. Kumar (2011), Wave-current interaction in Willapa Bay, *J. Geophys. Res.*, *116*, C12014, doi:10.1029/2011JC007387.

Oliveira, A., A.B. Fortunato, and J.R.L. Rego (2006), Effect of morphological changes on the hydrodynamics and flushing properties of the Óbidos lagoon (Portugal), *Cont. Shelf Res.*, *26*, 917–942, doi:10.1016/j.csr.2006.02.011.

Pires, H.N.O, and L.E.V. Pessanha (1986), Wave power climate of Portugal, in *Proceedings JUT AM Symposium, Hydrodynamics of Ocean Wave-Energy Utilization*, Lisbon, pp. 157–167.

Ranasinghe, R., C. Pattiaratchi, and G. Masselink (1999), A morphodynamic model to simulate the seasonal closure of tidal inlets, *Coastal Eng.*, *37* (1), 1–36.

Ranasinghe, R., and C. Pattiaratchi (1999), The seasonal closure of tidal inlets: Wilson Inlet—A case study, *Coastal Eng.*, *37*, 37–56.

Ris, R.C., and L.H. Holthuijsen (1996), Spectral modelling of current induced wave-blocking, in *Proceedings of the 25th Conference on Coastal Engineering*, Orlando, Florida.

Rusu, L., M. Bernardino, and C. Guedes Soares (2011), Modelling the influence of currents on wave propagation at the entrance of the Tagus estuary, *Ocean Eng.*, *38* (10), 1174–1183, doi:10.1016/j.oceaneng.2011.05.016.

Smith, R. (1975), Reflection of short gravity waves on a non-uniform current, *Math. Proc. Cambridge Philos. Soc.*, *78*, 517–525, doi:10.1017/S0305004100052002.

Soulsby, R. (1997), *Dynamics of Marine Sands: A Manual for Practical Applications*, Thomas Telford.

Swart, D. H. (1974), *Offshore sediment transport and equilibrium beach profiles*, Delft Hydraulics Lab., Publ. 131.

Suastika, K., M.P.C. de Jong, and J.A. Battjes (2000), Experimental study of wave blocking, in Proceedings of Coastal Engineering, Sydney, Australia, doi: 10.1061/40549(276)18.

Suastika, K. (2012), A spectral model for blocking of random waves, *Coastal Eng. J.*, *54* (2), 1250031-1-29, doi:10.1142/S0578563412500131.

Thomas, G.P. (1981), Wave–current interactions: An experimental and numerical study. Part 1. Linear waves, *J. Fluid Mech.*, *110*, 457–474.

Toledo, Y., T-W. Hsu, and A. Roland (2012), Extended time-dependent mild-slope and wave action equations for wave-bottom and wave-current interactions, Royal Society, UK, Proceedings.

Tolman, H. L. (2009), User manual and system documentation of WAVEWATCH III version 3.14. NOAA/NWS/NCEP/MMAB Technical Note 276, 194 p.

Tung, T. T., D. J. R. Walstra, J. van de Graaff, and M. J. F. Stive (2009), Morphological modeling of tidal inlet migration and closure, *J. Coast. Res.*, SI 56 (Proceedings of the 10th International Coastal Symposium), 1080 – 1084. Lisbon, Portugal, ISSN 0749-0258

Van Rijn, L. (1984), Sediment Transport, Part III: Bed forms and Alluvial Roughness, *J. Hydraul. Eng.*, *110*(12), 1733–1754, doi:10.1061/(ASCE)0733-9429(1984)110:12(1733).

Vincent, C. L., and W. D. Corson (1980), The geometry of selected US tidal inlets, GITI Report 20, U.S. Army Corps of Engineers, Washington, DC.

Westhuysen, A., M. Zijlema, and J.A. Battjes (2007), Nonlinear saturation-based whitecapping dissipation in SWAN for deep and shallow water, *Coastal Eng.*, *54*, 151–170, doi: 10.1016/j.coastaleng.2006.08.006.

Westhuysen, A. (2012), Spectral modeling of wave dissipation on negative current gradients, *Coastal Eng.*, *68*, 17–30, doi:10.1016/j.coastaleng.2012.05.001.

Winton, T.C., and A.J. Mehta (1981), Dynamic model for closure of small inlets due to storm-induced littoral drift, in *Proceedings, Congress-International Association For Hydraulic Research*, pp. 153–159.

Wolf, J., and D. Prandle (1999), Some observations of wave-current interaction, *Coastal Eng.*, *37*, 471–485.

Zhang, Y., and A.M. Baptista (2008), SELFE: A semi-implicit Eulerian–Lagrangian finite-element model for cross-scale ocean circulation, *Ocean Modell.*, *21*(3–4), 71–96, doi:10.1016/j.ocemod.2007.11.005.

Zhang, Y., R. Witter, and R. Priest (2011), Tsunami–tide interaction in 1964 Prince William Sound tsunami, *Ocean Modell.*, *40*(3–4), 246–259, doi:10.1016/j.ocemod.2011.09.005.